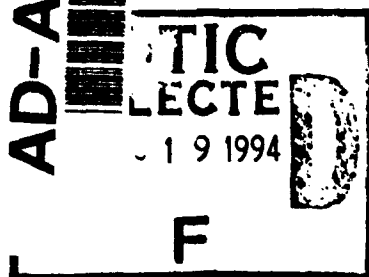


AD-A283 458



Semi-Annual Progress Report Number 2 on the Project entitled

Polarization-Difference Imaging: Biophysical Mechanisms and Engineering Applications to Visibility Enhancement in Scattering Media

Supported by

Office of Naval Research (ONR)
Perceptual Science Research Program

ONR Grant No: N00014-93-1-0935

Starting Date: July 1, 1993

Period Covered by This Report: October 1993-June 1994

Principal Investigators: Nader Engheta and Edward N. Pugh, Jr.

Student Members of The Research Team: Mickey Rowe, Eileen Lynch, J. Scott Tyo†

In the past nine months we have continued our work on *polarization difference vision and imaging* and their engineering potential applications to underwater observation and imaging of targets in scattering media. We have investigated various aspects of polarization-difference imaging (PDI) system and its features and characteristics. Moreover, we have studied polarization-sensitive vision in certain vertebrates, namely, green sunfish (*Lepomis cyanellus*) and pigeons (*Columba livia*). In the following sections, we report our findings in the past nine months in three projects related to polarization sensitive vision and imaging.

**Reverse Engineering of Polarization-Contrast Vision:
Polarization-Difference Imaging in Scattering Media**

In the past several months, the polarization difference imaging (PDI) project has had great success and taken off in exciting directions. One phase of the project was completed, a manuscript was prepared, and new experiments were designed and executed, all of which showed that PDI is a potentially powerful tool for observation of targets in scattering media. This part of the report will cover four main areas, viz., observation of metallic targets in scattering media, the development of an automatic rotational polarizer which improved the performance of the PDI system, the new experiments which are currently underway, and the theoretical work which is proposed for the near future.

1.1. Metallic Targets

At the end of last summer, we were testing the performance of the PDI system on several different types of targets. Initially, we had the idea of studying dielectric materials, such as plastics. When these targets are oriented at an angle with respect to the viewing direction they give rise to a preferential direction of polarization due to Brewster's angle phenomenon. This preferential polarization is usually difficult to pick up using conventional polarization-blind

† Mr. J. Scott Tyo was supported on this grant until May 17, 1994. Starting May 23, 1994, he has been supported by an NSF Graduate Research Fellowship and an Air Force Institute of Technology Sponsored Fellowship (Effective May 17, 1994 he has become a Second Lieutenant, US Air Force, and he is given AFIT Fellowship to continue his graduate study as a full-time student at the University of Pennsylvania). He was an undergraduate student in the Department of Electrical Engineering, University of Pennsylvania until May 19, 1994. Starting May 23, 1994, he has been a graduate student in our EE department continuing to work on his Master's thesis in our group on the project "Polarization-Difference Imaging". However, he is not supported on this grant since May 17, 1994.

94 8 18 187

94-26371



3978

1

systems, but we were able to use the PDI system to help detect these targets in scattering media when the performance of standard imaging techniques is poor. We had very good results when we tried to detect transparent targets, and we had limited success improving the detectability of translucent plastics.

After our initial experiments on dielectrics, we tried using the PDI system on metallic targets. When we used the PDI system to view dielectrics, we saw the light which passed out from the interior of the target. This light is called the diffuse component. Metallic targets are different, in that we see primarily the reflected light which virtually never makes it into the material. Each of these mechanisms (reflection and diffusion) serves to create a partial polarization in a different way, but once the light leaves the target, it is no longer crucial how the light was polarized, only that it is and whether it can be detected by our detector. We first found that metallic targets also partially polarize the light, but they were so visible under the conditions of our experiments that the PDI system was not providing an additional advantage to improve the detectability of the target relative to the background. However upon further experimentations we found a very interesting property of the PDI system in detecting surface features of metallic targets:

As an experiment, we tried scratching the surface of the metallic target to see what the effects were. What started out as something of an unknown turned into a huge success. The scratched surfaces of the targets acted as small facets, each of which was oriented in a slightly different way. All of these facets together gave rise to a collective polarization which we were able to detect using the PDI system. Interestingly, these scratches were practically impossible to detect using standard polarization-blind imaging systems and procedures. However, using the PDI system we were able to detect them. Appendix A contains a preprint of our manuscript describing our imaging system and experimental setup along with results showing the advantage of polarization-difference imaging. Figure 1 presents sketches of experimental setup for such targets. The striking outcome of the PDI system observing such metallic targets is shown in Fig. 2 of the preprint attached in Appendix A.

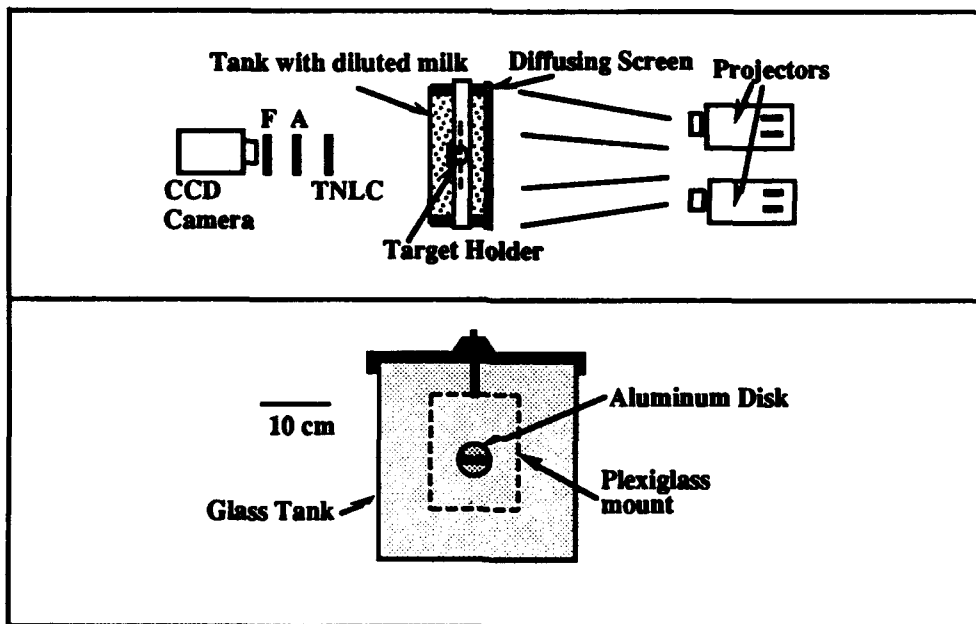


Fig. 1. Top panel depicts the top view of the experimental setup for our PDI System. A: Polarization analyzer; TNLC: twisted nematic liquid crystal; F: narrow-band filter. Bottom panel shows the front view of the tank (drawn to scale) with inside dimensions 30cm x 30cm x 15cm. This tank is filled with water to which milk is added. The target is suspended in the middle of the tank. The experimental results of PDI system are shown in Fig. 2 of the preprint in Appendix A.

For	
DRA&I	<input checked="" type="checkbox"/>
FAB	<input type="checkbox"/>
anced	<input type="checkbox"/>
ion	
Ability Codes	
avail and/or Special	
A-1	

1.2. Automatic Rotational Polarizer (ARP)

As his Senior Undergraduate EE Design Project, Mr. J. Scott Tyo (one of the student members of our research team) designed and built an Automatic Rotational Polarizer which improved the performance of our PDI system. We noticed two problems which came up consistently in the PDI system which we decided to address. The first problem was a motion artifact that was due to the rotating of our linear polarizer. This artifact was manifested as dark and light bands around the edges of the metallic target. The second problem was that the background light may not be randomly polarized as it was in our early experiments. If the background polarization is not compensated for, the performance of the PDI system can be diminished.

The first problem was solved using a twisted nematic liquid crystal (TNLC) cell. This cell serves as a polarization rotator and can be controlled electronically. When there is a voltage applied across the cell, it does not affect the polarization of the incident light, however, when the cell is not electrically excited, the polarization of the light leaving the cell is rotated ninety degrees with respect to the incident light. We can take advantage of the two states of the TNLC to capture out vertically and horizontally polarized images without mechanically manipulating the system. The introduction of the TNLC solved our motion artifact problem and it was used to prepare the images which were presented in Fig. 2 of the preprint attached in Appendix A.

In order to compensate for the background polarization problem, a stepper motor was introduced. The TNLC allowed us to capture images polarized parallel and perpendicular to our analyzer, and the stepper motor rotated our analyzer, thus rotating the direction of polarization being used to create PD images. When the background light is not randomly polarized, its preferential polarization can be represented as a vector pointing in a given direction (This is in fact the direction of the major axis of the polarization ellipse of polarized part of the background light). In order to null out this background polarization effect in the PDI system, the analyzer must be oriented so that it makes a 45 degree angle with respect to the major axis of polarization ellipse of the background. The stepper motor assembly and circuitry has been designed, built, and tested, but it has not been used yet in creating images for presentation.

1.3. Limit of Detectability: Application of Signal Detection Theory

The PDI system has been shown to improve the detectability of target features in scattering media (See Fig. 2 of Appendix A). We have observed such improvement qualitatively, and we need to develop some quantitative way of describing the advantages of PDI in enhancement of target detection under certain circumstances. In the areas of signal processing, communications, and psychophysics, there is often the need to quantify the performance of a given receiver. There has been a lot of work reported in the literature in the area of signal detection theory (SDT) [For example, David M. Green and John A. Swets, *Signal Detection Theory and Psychophysics*, John Wiley and Sons, Inc., NY 1966.]. SDT breaks a given target (or stimulus or signal) detection process down into the probabilities for various events to occur, such as hits, false alarms, misses, and correct rejections. Obviously, the performance of a given system can be quantified, and in this way different systems can be compared. In addition, an ideal observer model is usually employed [For example the work by W. S. Geisler, "Sequential Ideal-Observer Analysis of Visual Discriminations" *Psychological Review*, vol. 96 No. 2, 1989, pp. 267-314.] which takes into account only the information which is received, not any post-receiver operations which may occur to degrade a given signal's detectability.

We are in the process of applying the SDT approach to test the following hypothesis about our PDI system: PDI system can have a higher probability of detecting a target in a scattering medium than standard imaging systems under certain conditions. These conditions include many different situations where the signal is just at or below threshold levels.

Obviously, if standard imaging system can easily detect a signal, the PDI system is not of high priority. However we would like to show that there are cases where standard imaging procedures do not perform as well as PDI system does, and these cases may be the ones with situations at the threshold of detectability. These conditions may include, but are not limited to, environments where scattering particles are present in the viewing medium, and limit an imaging system's performance and lighting patterns that have significant background variations. These conditions occur in a variety of environments, but two of the most common are underwater and foggy environments. It must be noted that such possible enhanced detectability for PDI system appears to be in addition to the common-mode rejection capability of PD imaging. The common-mode rejection can even further improve the detectability of targets in scattering media. (See Fig. 2 in Appendix A)

In order to test this hypothesis, the following experiment has been proposed and is in the early stages of implementation. Using the setup described in Appendix A, we choose a given milk concentration. Without changing anything about the system, we collect a series of vertically and horizontally polarized images. From these images, create the appropriate polarization-sum (PS) and polarization-difference (PD) images. We will repeat the procedure with a second aluminum target which is sandblasted but does not have the scratched patches. The first set of data represents the signal plus noise distribution while the second represents the noise alone (or non-target) distribution. Once all the data is collected, we will study the distributions of various variables, such as absolute intensity, difference between different regions, difference from the mean, etc., for each case. By plotting these distributions, SDT can be used to analyze the data and test the hypothesis.

1.4. Proposed Theoretical Work for PDI System

There is a large body of literature which deals with propagation and radiation in scattering and random media [For example, A. Ishimaru, *Wave Propagation and Scattering in Random Media*, vols. 1 and 2, Academic Press, NY, 1978; Y. Kuga and A. Ishimaru, "Imaging of an Object Behind Randomly Distributed Particles Using Coherent Illumination," *J. Wave Material Interaction*, Vol. 3, No. 2, pp. 105-112, April 1988; and H.-W. Chang and A. Ishimaru, "Beam Wave Propagation and Scattering in Random Media Based on the Radiative Transfer Theory," *J. Wave-Material Interaction*, Vol. 2, No. 1, pp. 41-69, January 1987]. Some of these methods may be employed to study the physics of the PDI-system experiments presented here. Specifically, we must study the depolarization of a polarized ray of light and the selective polarization of a randomly polarized ray of light. Both of these phenomena are due to, amongst other things, directional scattering of light within the scattering medium. We would like to study ways of analytically justifying the results which we obtain from the SDT experiments. This justification will probably come out of the scattering medium work, but new methods may also be employed.

Biophysical Basis of Polarization Sensitivity in Teleost Fish

The goal of this part of the research program is to test the hypothesis that sunfish double cone photoreceptors behave as birefringent waveguides, and thus provide the mechanism by which these fish detect polarization of light. In previous work, (See Appendix B for a reprint of our previous work) electron microscopic analysis of sunfish cone inner segments led to the hypothesis that the inner segment region of the receptors are graded index waveguides. During this reporting period we collected data to test that hypothesis as directly as possible given currently available technology.

One of us (Mickey Rowe who is one of our graduate students from The Institute of Neurological Science at the University of Pennsylvania) made three trips to the Duke University Medical Center in Durham, North Carolina to collect interferometric data from sunfish cones.

He collected the data in the laboratory of Dr. Joseph Corless, whose modified Vickers M85 microscope made the data collection possible.

2.1 Scanning Interferometry

After the sunfish's retina is obtained, it is left in a Ringer's solution similar to that used by Dearry and Burnside [A. Dearry and B. Burnside, "Effects of Extracellular Ca^{++} , K^{+} , and Na^{+} on Cone Retinal Pigment Epithelium Retinomotor Movements in Isolated Teleost Retinas", *J. General Physiology*, Vol. 83, pp. 589-611, 1984]. It was discovered during the third trip that the best results were obtained by shaking the retina in the solution, and pipetting a small volume (8 μl) of fluid from the surrounding solution. It was also discovered just prior to the third trip that the largest number of cones could be obtained by killing the fish 2-3 hours into its subjective night after the fish had been in complete darkness for at least 26 hours. During the first two trips very little data were collected due mainly to problems with the dissection.

The Vickers M85 microscope's operation can be briefly described as follows: light from a He-Ne laser (wavelength 632.8 nm in free space) is split into two beams, a scanning beam and a reference beam. The beams travel in parallel through the microscope's optical system until after they have passed through the sample plane in which the photoreceptors reside. While travelling through the sample plane, one of the beams passes through a photoreceptor of interest, and the other beam passes through the solution adjacent to the receptor. Passage through the photoreceptor retards the scanning beam, so that when the two beams are recombined beneath the sample plane, the scanning beam is shifted in phase relative to the reference beam. The microscope is designed to measure this phase shift and thus determine the optical path length of the section of the photoreceptor traversed by the beam. For these experiments, the beam was reduced to a spot size of approximately 0.3 μm as it passed through the photoreceptor. During an experiment the beams are moved in a raster pattern in the sample plane, with 0.22 μm between measurements. Data are thus collected as a two dimensional matrix of points (see Fig. 2).

The data collected as described in the preceding paragraph represent the additional optical path length (opl) travelled by the scanning beam relative to that travelled by the reference beam. This opl is related to the refractive index via: $\text{opl}(x,z) = \int_y \delta n(x,y,z) dy$.¹ (See Fig. 2 for an explanation of the coordinate system used throughout this section.) For this project we are interested in extracting $n(x,y,z)$ from our data.

Although our goal is to understand the biophysics of the double cones, we have focused our efforts on analyzing data collected from single cones because they can be assumed to be radially symmetric. This assumption of radial symmetry allows us potentially to extract $n(x,y,z)$ from a single matrix of $\text{opl}(x,z)$ data. The previous evidence which lead us to propose a gradient index model of the double cones applies equally well to the single cones. If it can be shown that the single cones possess an index profile graded as we have hypothesized, then we can infer that the double cones have a graded index profile as well.

¹ The δ in this and subsequent equations signifies a difference between the refractive index of the object under study, and the Ringer's solution in which the object is immersed. The Ringer's solution had a measured refractive index of 1.3351, and this constant can be added to any of the δn 's to convert them to absolute refractive indices.

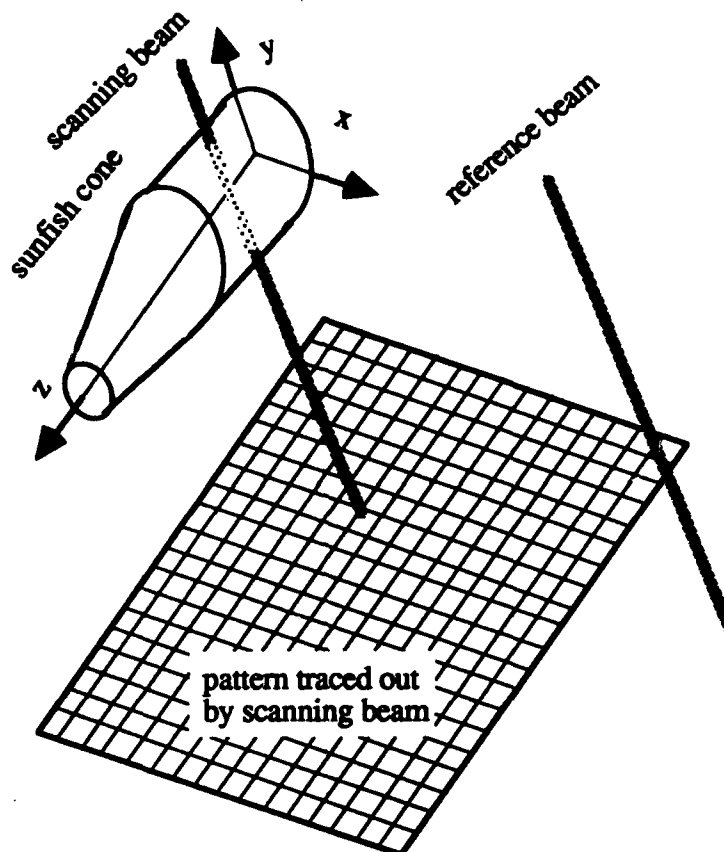


Figure 2. Diagrammatic representation of scanning interferometry. The scanning and reference beams are moved in a raster pattern in order to collect a two-dimensional matrix of data samples. At each data point, the phase difference between the scanning and reference beams indicates the additional optical path traveled by the scanning beam as it travels through the cone or other specimen of interest.

2.2 Preliminary Results

In our data analysis we have made some simplifying assumptions, chiefly that the scanning beam passes through our samples as diagrammed in Fig. 2. In reality, the scanning beam is too narrow to be treated as a pencil of light--because the spot is focused to a point smaller than the light's wavelength, the "beam" must be diverging at the sample plane. The microscope is designed well enough (e.g. with appropriately placed apertures) that this may not affect the calculations presented below, but we are in the process of performing some additional calibrations to test the validity of this assumption. Even if the light hitting the sample was a straight beam, refraction at the interface should cause the beam to bend as it enters the cones at all positions except the midline ($x = 0$, where the light impinges normally on the surface). With preliminary analyses based on a homogeneous refractive index model this bending was found to be minor, and it is thus reasonable to ignore it at this stage of calculation. Furthermore, the increased pathlength at the periphery of the cell would cause that region to appear to have a larger refractive index than it does, and thus would bias our results away from the conclusion we are attempting to support.

Given the assumptions that the single cones are radially symmetric around their z-axes, and that the scanning beam passes through them as an undeflected pencil of light, we can extract $n(x,y,z)$ from $opl(x,z)$ in at least two different ways. The way that we have concentrated upon during this reporting period is to begin with models of $n(r,z)$ (where $r = \sqrt{x^2 + y^2}$), determine the theoretical $opl(x,z)$ which would result, and calculate the difference between the data and this model and square that difference. We then adjusted parameters of the model and found the squared error again. This procedure was repeated until a minimum in the difference between data and theory were obtained. Prior to fitting, however, the data were made symmetrical. Since we are assuming radial symmetry, it should be true that: $opl(x,z) = opl(-x,z)$. We thus treated the data on either side of the z axis as independent estimates of the actual value. In order to appropriately average the data, we had to determine where $x = 0$. We did this independently for

each value of z in our data set by maximizing $\int opl(x) \cdot opl(-x)dx$ as the position where $x = 0$ was moved across the data slice. Since our data is discrete and the position where $x = 0$ might not fall on a pixel, data were interpolated prior to averaging. The resulting "symmetrized" data were used in all subsequent calculations. The first index model tested was:

$$\text{homogeneous:} \quad \delta n(x:z) = \begin{cases} \delta n_{\max} & |x| \leq R \\ 0 & \text{else} \end{cases}$$

The homogeneous model has two parameters, δn_{\max} and R, the refractive index within, and the radius of the cell respectively. Note that both parameters are potentially functions of z. The second model tested was:

$$\text{parabolic:} \quad \delta n(x:z) = \begin{cases} \delta n_{\max} \left[1 - \left(\frac{x}{R} \right)^2 \right] & |x| \leq R \\ 0 & \text{else} \end{cases}$$

This model also has two parameters, but in this case δn_{\max} is the refractive index increment at the center of the cell and R specifies not only the outer border of the cell, but also how fast the index declines as a function of r.

Overall, the data were better fit by the homogeneous model than the parabolic model. However, when the models were compared point by point it was determined that around $x = 0$, the parabolic model over-estimated the opl and the homogeneous model under-estimated it. Nearer to the perimeter of the cells the situation was reversed: the parabolic model tended to under-estimate the opl while the homogeneous model over-estimated it. For this reason we chose to pursue a three-parameter model:

$$\text{power-law:} \quad \delta n(x:z) = \begin{cases} \delta n_{\max} \left[1 - (x / R)^\alpha \right] & |x| \leq R \\ 0 & \text{else} \end{cases}$$

The power-law model is a more general expression of the two particular models already described. The power-law model reduces to the homogeneous model when $\alpha = \infty$, and to the parabolic model when $\alpha = 2$. For intermediate values of α , the index profile has a shape intermediate between the two previous cases. After fitting the power-law model to the data, the

values for n_{avg} , R , and α were plotted as a function of z . Figure 3 shows the results of these calculations along with the results from the homogeneous model for one cell.

The programs currently used to find the best fits for the power-law model run very slowly. The cell depicted is currently the only one for which the analysis has been completed. However, for the homogeneous model, several other cells have been tested. The general trend displayed in panel A of Fig. 3 is evident in nearly all of these cells. That is, the refractive index is lower near the base of the photoreceptor inner segment than it is near the base of the outer segment, and it rises monotonically in between. This pattern provides confirmation of a prediction made previously based on electron microscopy alone (Our paper in Appendix B). The sharp drop in index at the outer segment is unexpected, and may be the result of post-mortem pathology; the outer segment is more fragile and thus more sensitive to trauma imposed by the dissection procedure than is the inner segment. Panel B depicts the dependence of the cell's radius on z . The values obtained via this method are similar to light microscopical measurements of fixed and stained retinas (D. A. Cameron and E. N. Pugh, Jr., *Nature*, vol. 353, 161-164, 1991; and D. A. Cameron and S. S. Easter, Jr., *Vision Neuroscience*, vol. 10, 375-384, 1993). Panel C of Fig. 3 provides support for the prediction we set out to test. Two anticipated points are demonstrated in that panel: 1) the cell is best fit by values of α less than infinity. If the cell really had a homogeneous refractive index then one would predict that no minimum error would be found--the error in the best fit would continue to decline as higher values of α were tested. 2) The best fit α increases as a function of z . This is in accord with previous observations based on electron microscopy.

For a quantitative evaluation of the fits for the homogeneous versus power law models, the error functions were plotted as a function of z . As described above, the error between the data and the model were determined by finding the opl which would result from a model having the parameters depicted in Fig. 3, subtracting those values from the symmetrized opl data, and then squaring the resultant number at each point (x, z). These numbers were then summed along x to show the error only as a function of z . Fig. 4 portrays the residual errors after the best fits were obtained for the two types of model. Note that the errors are plotted on a logarithmic scale. The errors have not been normalized--the errors seem to climb as a function of z , but this may result from the fact that the raw numbers in the data increase as a function of z . However, the important point to note is that the power-law model tends to fit the data around ten times as well as the homogeneous model along most of the photoreceptor inner segment's length.

Another method for extracting $n(r, z)$ from $opl(x, z)$ is to perform an inverse Abel transform of the data. The Abel transform is a special case of the Radon transform used in medical imaging. It can be shown that if δn is radially symmetric, it can be reconstructed according to Barrett and Swindell³:

$$\delta n(r) = -\frac{1}{\pi} \int_r^\infty \frac{d(opl)/dx}{\sqrt{x^2 - r^2}} dx$$

where in our calculation the upper limit is approximately taken to be R which should be obtained from the data. The difficulty in applying this method is that $d(opl)/dx$, and R must be extracted from the data. For one scan line of the same cell whose analysis is depicted in Figs. 3-4, we have

-
- ² δn_{avg} is related to δn_{max} in the power-law model via: $\delta n_{avg} = \delta n_{max} \frac{\alpha}{(\alpha + 2)}$. This can be shown by integrating $\delta n(x)$ from $-R$ to R , and dividing by πR^2 .
- ³ H. H. Barrett and W. Swindell, *Radiological Imaging: The Theory of Image Formation, Detection, and Processing*, vol. 2, Academic Press, NY, 1981, p. 406.

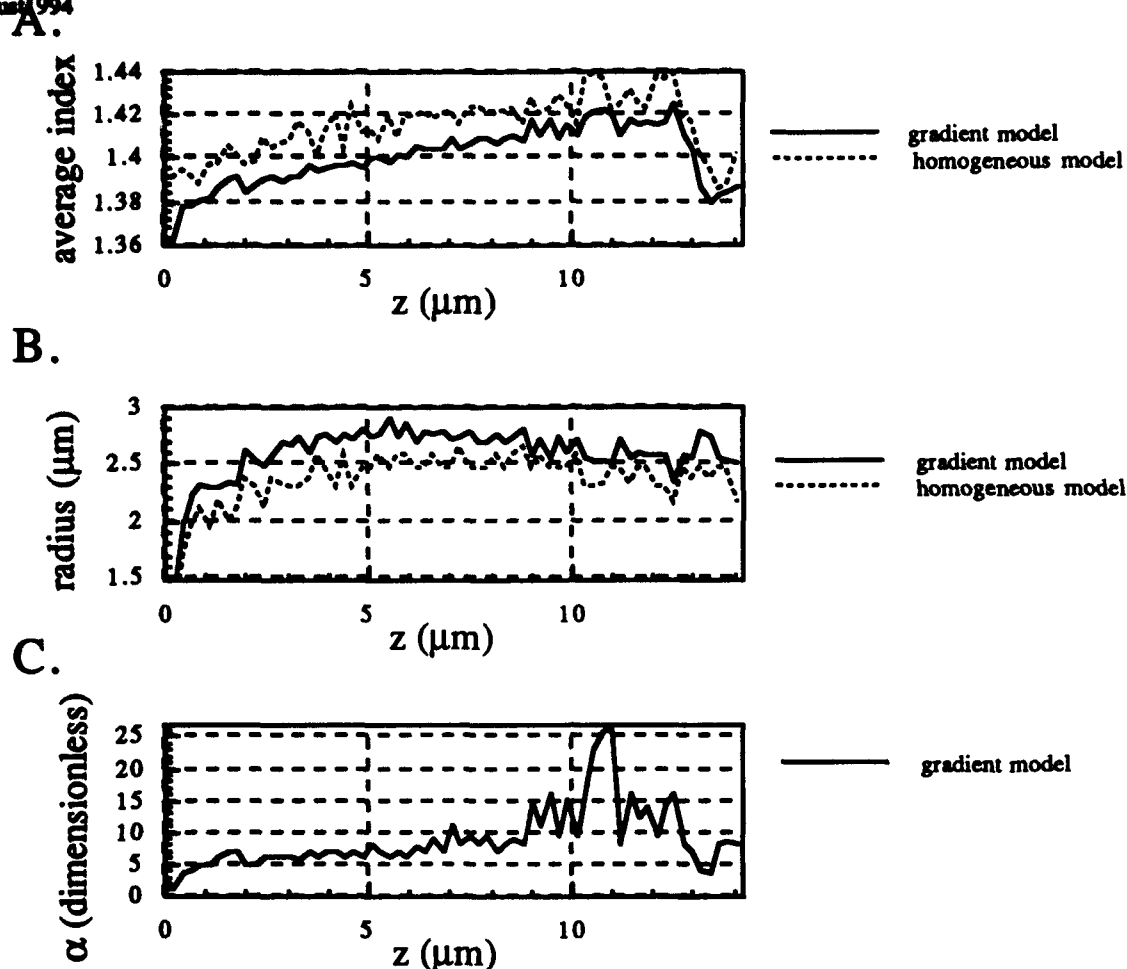


Figure 3. Best fit parameters for the homogeneous and power law models of the refractive index of a single cone. A. Average refractive index within the single cone as a function of distance from the base of the inner segment. The large drop near $z = 14\mu\text{m}$ is the junction between the inner and outer segment of the photoreceptor. B. Radius of the cone. C. For the power-law model, the exponent specifying how fast n decreases.

performed this calculation by fitting the opl data to a spline curve, calculating the derivative from this spline,

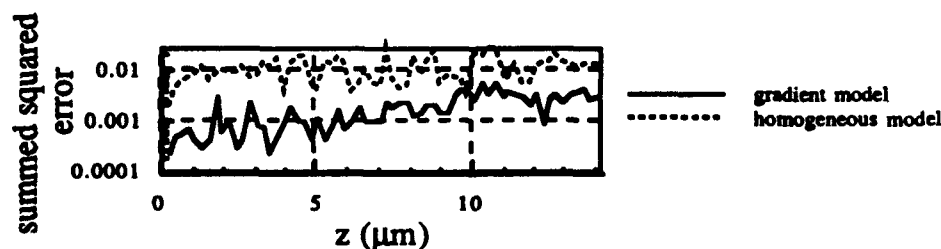


Figure 4. Residual error between models and data. For each point along the z -axis, optical path lengths were calculated as a function of x to best fit the data. The difference between the calculated opl's and the symmetrized data were then found as a function of x . The differences were then squared point by point and the resultant squared error summed over x . These values are here plotted as a function of z for the homogeneous and power-law models.

and then defining R as the appropriate zero crossing of the $d(\text{opl})/dx$ curve. The resulting plot of $n(r)$ is depicted in Fig. 5 with the $n(r)$ determined from the power law-model fit included for comparison.

At this time it is not clear whether the small central rise in $n(r)$ as determined by the inverse Abel method is an accurate reflection of the underlying refractive index profile, or whether it is an artifact of the reconstruction technique. One line of evidence suggesting that the hump is real (and therefore that the power-law function we are using is incapable of faithfully recovering the true index profile) is that when the best fit opl is subtracted from the data, the model still seems to underestimate the center and overestimate the perimeter. Further analysis of the data will hopefully determine if another model can fit the data better than the power-law function.

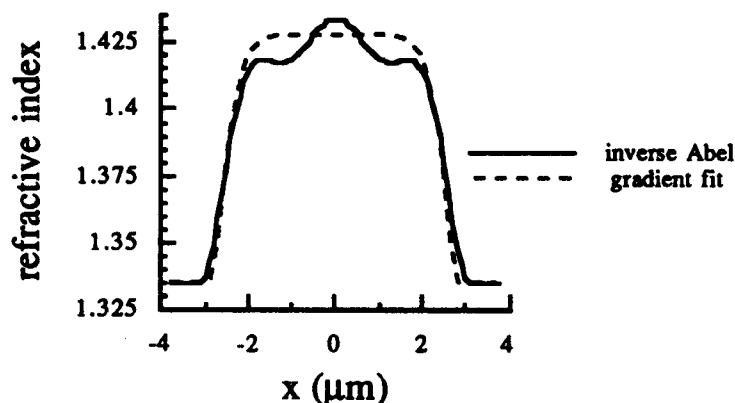


Figure 5. $n(r)$ was reconstructed from $\text{opl}(x)$ for one scan line of the cell analyzed for Figures 2-4. The reconstruction was done in two ways. The solid curve results from applying the inverse Abel transform on the symmetrized data. The dotted curve is from the best fit with a power-law model. The scan line in question is for $z = 8.36 \mu\text{m}$.

2.3 Behavioral Experiment of Polarization Sensitivity of Green Sunfish

We have initiated work on behavioral experiments studying sensitivity of green sunfish's visual system to the polarized light. An undergraduate student, Ms. Kara Ko has joined our group over the summer to work, along with our graduate students, in this part of the project. We are exploring several possibilities, namely, the ability of fish to discriminate between linearly polarized light and circularly polarized light, to discriminate between vertically and horizontally polarized light, and also to discriminate between monochromatic lights with differing wavelengths. Experimental setup is being prepared for measurement of electroretinographic (ERG) signals from fish's eye when it is illuminated by flashes of light.

Biophysical Basis of Polarization Sensitivity in Pigeons

Modifications and improvement of new apparatus for pigeon experiments (for lateral testing) and the original (frontal) were completed in September 93. The computer programs necessary to run this new apparatus were written. Tests on one bird were run on the frontal contrast paradigm. In this contrast paradigm, two possible stimuli were the patterned field (i.e., left half of rectangular field was black and the right half was white), and the homogeneous field (i.e., left part was white, and the right part was also white with a black line separating the two fields). The homogenous field was S_+ and the patterned field was S_- . This paradigm was used for two reasons: 1) we needed a control for the experiment we ran last year, in which the S_+ was the patterned field and S_- was homogenous one; and 2) we needed more subjects run in this experiment. We did not think that one subject was enough. The results were comparable to that run in the previous year (For 70 % of the trials, the performance of the bird was correct when the contrast between the two sides of the test field was around 21 %.)

One bird was run on the lateral testing paradigm. From October 19 -November 15, this bird was trained to peck at the orienting key. Initially, one peck was resulted in the food reward. The number of pecks needed was slowly increased. Eventually, we paired the orienting key with S_+ test field presentation. So, both were simultaneously illuminated. It was hoped that the animal would happen to look down the side channel while pecking the orienting key. Once the animal learned this task, testing was begun. It turned out that it was very difficult to perform such tests. The main reason was because we were not certain that the animal was looking down the test channel. In an attempt to make the orienting key serve as an indicator of when to "look" down the test channel, we gave it primary importance over the channel. The "strength" of the orienting key as a signal to when food was going to be presented overrode the importance of looking down the test channel to examine the state of the test field.

In February, a couple of different methods were used in order to get the birds to pay more attention to the test channel. First, we increased the no-reward option if the animal pecked during the S_- condition. This didn't work. Next, we decided that keeping the orienting key steadily illuminated was a better method of testing the animal. In this way the state of the orienting key did not change, but the state of the channel did. First, a tone was added to signal the presentation of the test field. So, while the animal was pecking at the orienting key, two 250-ms tone burst were emitted from a location directly above the test field. 500-ms after the second tone burst, the test field was turned on. During the S_- stimulus presentation, the holder which mounts either the polarizer or quarter-wave plate is rotated. In the S_+ condition, the field is held constant. For two birds, a contrast paradigm was used, so the S_+ was the steady homogeneous (white) field and the S_- was the rotating field. For one bird, the S_+ was the circularly polarized field, and the S_- was the rotating polarization field. The plates rotated at 0.6 Hz. During S_- presentation, the animal was supposed to inhibit pecking. If the bird pecks the key the same number of times as required in the S_+ condition, it is sent into a no-reward phase. In the no-reward phase, a loud 500-ms tone immediately follows each additional peck in order to call attention to the lateral field and illustrate that pecking during this stimulus state was unwanted. The birds began showing some inhibition in this paradigm, but the difference in pecking rates did not vary enough between the two stimulus conditions.

In the middle of March we changed the design of the experiment once again. The main difference occurs during the S_- presentation. Basically, we have added some training S_- trials. Training trials are concentrated in the beginning of the experimental session, with a few scattered in the middle and the end. In training trials, two pecks at the orienting key sends the animal into the no-reward phase described above. The purpose of these trials is to extinguish pecking to S_- early in the experimental session. All three birds were tested using the rotating contrast paradigm just described above. The one bird was switched over from the pure polarization

paradigm because we thought it was a much harder task, and wanted to get her to attend to the lateral field. All three birds are showing significant inhibition during S₋ presentation. The pecking rates during S₊ and S₋ conditions are statistically significant.

The problem with this experiment is that the rotating mount serves as an audible cue for the animal. We are presently trying to eliminate this as a cue. What we want to do is to have the mount rotate in both conditions because we think that a flickering stimulus may be easier for the animal to detect. Recently, we bought a motor which enables us to rotate the stimulus at a flicker rate up to 10-Hz. However, we have been unable to implement this new procedure because of the physical features of the light. In order to move the rotatable mount during the homogeneous field presentation, the light must be 100% circularly polarized before it reaches the rotating polarizer. However, due to optical constraints, we have not yet been able to achieve this. As a result, the stimulus state is not static as we rotate the polarizer. We are currently attempting to solve this problem.

APPENDIX A

Preprint of the Manuscript entitled

POLARIZATION-DIFFERENCE IMAGING (PDI): A BIOLOGICALLY INSPIRED TECHNIQUE FOR OBSERVATION THROUGH SCATTERING MEDIA

Authors: M. P. Rowe, J. S. Tyo, E. N. Pugh, Jr., and N. Engheta

POLARIZATION-DIFFERENCE IMAGING (PDI): A BIOLOGICALLY INSPIRED TECHNIQUE FOR OBSERVATION THROUGH SCATTERING MEDIA

M. P. Rowe[†], J. S. Tyo^{*}, E. N. Pugh, Jr.^{°†}, and N. Engheta^{*}

[†]Institute of Neurological Sciences
University of Pennsylvania
Philadelphia, PA 19104

^{*}Moore School of Electrical Engineering
University of Pennsylvania
Philadelphia, PA 19104

[°]Department of Psychology
University of Pennsylvania
Philadelphia, PA 19104

ABSTRACT

Many animals have visual systems that exploit the polarization of light, and some of these systems are thought to compute difference signals in parallel from arrays of photoreceptors optimally tuned to orthogonal polarizations. We have hypothesized that such "polarization-difference" systems may improve the detectability of objects in scattering media by reducing the effectiveness of background light whose degree of linear polarization is different from that of the objects. Here we present experimental results which demonstrate that a man-made polarization-difference imaging system can enhance the visibility of features of a target in a scattering medium. Specifically, we show that surface features of a metallic target invisible to conventional imaging are readily visible with polarization-difference imaging.

Optical scattering by suspended particles (e.g. fog, rain, plankton) is well known to diminish the visual contrast of objects.¹⁻³ Although polarization-sensitive vision is well documented as serving in navigation^{1,4,5}, some types of polarization-sensitive vision may also serve to enhance the visibility of targets in scattering media.^{6,7} The goal of this Letter is to demonstrate that a man-made polarization-difference imaging (PDI) system similar to that hypothesized to function in some biological visual systems^{7,8} can indeed enhance the visibility of target features in a scattering medium.

Our PDI system captures images of a given scene at two orthogonal linear polarizations, computes the difference of the images pixel-by-pixel, and re-scales the resultant difference-image for optimum use of the display range. Symbolizing the two image intensity distributions as $I_{\parallel}(x,y)$ and $I_{\perp}(x,y)$, where (x,y) identifies the pixel position in the image and \parallel and \perp indicate two orthogonal linear polarizations defined below, the PDI system generates the *polarization-difference (PD) image*

$$pdI(x,y) = I_{\parallel}(x,y) - I_{\perp}(x,y). \quad (1a)$$

The system also computes the *polarization-sum (PS) image*

$$psI(x,y) = I_{\parallel}(x,y) + I_{\perp}(x,y). \quad (1b)$$

For an ideal linear polarizer, the PS image is equivalent to a polarization-blind image obtained by a conventional imaging system. We define the local "observed degree of linear polarization" by

$$ODLP(x,y) \equiv pdI(x,y)/psI(x,y). \quad (2)$$

The quantity $\langle ODLP \rangle_{\text{region}} = \langle pdI(x,y) \rangle_{\text{region}} / \langle psI(x,y) \rangle_{\text{region}}$ serves as a dimensionless measure of the observed PD magnitude in a particular image region. In general, both $pdI(x,y)$ and $ODLP(x,y)$ depend upon the choice of polarization axes; $psI(x,y)$, however, does not.

The experimental layout is sketched in Fig. 1. Two incandescent tungsten filament slide projectors back-illuminate a sheet of 0.25" thick white plexiglass attached to one face of a glass tank. The tank is filled with water to which milk is added. The plexiglass acts as an initial diffuser and the milk as a scattering agent. A CCD camera (Hamamatsu, model XC-77) views the tank through the clear glass face. In the absence of a target, the radiance of the tank is nearly

uniform across the viewing area, and is essentially randomly polarized. The target used for the experiments reported here is an aluminum disk. The target is suspended in the middle of the tank by means of a rod attached to the disk face occluded from the camera. The rod is attached to a clear plexiglass mount suspended from above; the surface of this mount is perpendicular to the incident light, and both it and the rod attached to the disk are undetectable to both PDI and conventional imaging. The disk surface facing the camera is sandblasted, rendering it nearly Lambertian everywhere, except for two 1-cm² patches. These patches are raised a few thousandths of an inch and have been abraded with emory paper lightly in orthogonal directions -- on one patch roughly radially, and on the other roughly tangentially. The camera is equipped with a macro lens (Vivitar Y/C 55 mm f2.8) and forms an image of the target plane (see Figure 2); images are digitized and processed with an image analysis system (Series 151, Imaging Technology, Inc.). Before reaching the camera, the light from the tank passes through a twisted nematic liquid crystal (TNLC--Liquid Crystal Institute, Kent State U.) In its off state the TNLC rotates the plane of polarization of incident light by 90°; when driven, the TNLC passes the incident light with no rotation. After the TNLC, the light passes through a linear analyzer. Since the TNLC's behavior is wavelength-dependent, a narrow-band filter (10 nm full-width at half maximum, centered at 610 nm) serves to eliminate light out of the TNLC's operating waveband. The TNLC/analyzer combination selects the orthogonal axes of the polarization-difference image as follows: when the TNLC is driven, the TNLC/analyzer passes only light polarized *parallel* to the analyzer axis, yielding the image $I_{||}(x,y)$; when the TNLC is off, the TNLC/analyzer combination passes light polarized *perpendicular* to the analyzer axis, yielding $I_{\perp}(x,y)$. For the results reported here, the analyzer axis was oriented vertically.

Figure 2 illustrates the application of the PDI system to the aluminum target suspended in diluted milk. Panels A and B present the images, $I_{||}(x,y)$ and $I_{\perp}(x,y)$, convolved with a two-dimensional (low-pass) filter. Panels C and D represent the sum and difference images. Panels E and F present the data in images in C and D, but now scaled to utilize the full 8-bit intensity range of the display. The abraded patches, which are not visible in Panels A, B and C (the raw

and sum images) are clearly visible in the scaled PD image (Panel F), but barely visible in the scaled PS image (Panel E). Panels A' - F' present numerical plots (as a function of x) of average pixel intensities in the vertical bands between the arrows shown in A - F; these plots provide quantitative evidence supporting the qualitative conclusion drawn from inspection of the images, viz., that the abraded patch regions are most distinct from the disk background in the scaled difference image (F, F').

The principal factor underlying the enhanced visibility of the two patches in Panel F is the common-mode rejection feature intrinsic to PDI. Given that a target or target feature produces a non-zero value of $\langle \text{ODLP} \rangle$ in some region (Eq. 2), the system enables extraction of this feature by "rejecting" intensity "common" to both polarization axes. This common-mode rejection feature of the PDI system is exhibited in two ways in the images of Fig. 2: firstly, the relatively intense halo of unpolarized light surrounding the disk is eliminated (cf. C' and D'), and secondly, the relatively modest (ca. 20%) intensity variation across the disk surface is also minimized, allowing higher gain to be applied to the final displayed PD image (cf. E' and F').

Based on the results shown in Fig. 2 and others we have obtained, PDI can be argued to have a very general applicability. Firstly, our results show that PDI is quite sensitive to small signals. For the left abraded patch in Fig. 2, $\langle \text{ODLP} \rangle = 0.0164$; for the right patch, $\langle \text{ODLP} \rangle = -0.0138$. Moreover, in experiments in which we systematically raised the milk concentration to degrade the images until the target patches were undetectable, a target patch having $\langle \text{ODLP} \rangle < 0.01$ could still be easily detected in the PD image (data not shown). The images of great many object surfaces in natural environments predictably will have ODLPs of considerably higher magnitude.⁹

Secondly, PDI generalizes readily to scattering environments in which the "background" itself has some degree of linear polarization. Judicious selection of the orthogonal polarization axes of the PDI system can enhance the ODLP of target regions relative to that of the background in the image plane. One of us (J. S. Tyo, EE Senior Design Project) has produced a system that automatically finds the polarization axes that minimize the ODLP under "background

alone" conditions; once $\langle \text{ODLP} \rangle_{\text{background}}$ is minimized, maximum display gain can be automatically introduced, and targets having an ODLP different from the background readily "pop out."

Finally, PDI also possesses the generally useful qualities of being passive, simple and potentially very fast. PDI can operate passively in any region of the electromagnetic spectrum in which natural radiation exists. PDI is simple, in that it does not require the use of sophisticated image processing techniques (but of course, any image processing techniques can be added to, or used in parallel with PDI to make it even more effective). PDI is also potentially very fast, inasmuch as it can be implemented in a massively parallel system, as nature appears to have done in the retinas of many animals.^{7,8,10}

This work is supported by US Department of Navy, Office of the Chief of Naval Research Grant No. N00014-93-1-0935, and, in part, by the University of Pennsylvania Research Foundation.

References:

- [1] J. N. Lythgoe, *The Ecology of Vision*, Oxford University Press, London (1979).
- [2] S. Q. Duntley, *J. Opt. Soc. Am.* **53**, 214-233 (1963).
- [3] S. Q. Duntley, in *Optical Aspects of Oceanography*, N. G. Jerlov and E. Steemann Nielsen, eds., (Academic Press, New York, 1974), pp. 135-149.
- [4] K. von Frisch, *Experientia*, **5**, 142-148 (1949).
- [5] T. H. Waterman, in *The Handbook of Sensory Physiology Vol. VII/6B Vision in Invertebrates*, H. Autrum, ed., (Springer-Verlag, New York, 1981), pp. 281-469.
- [6] J. N. Lythgoe and C. C. Hemmings, *Nature*, **213**, pp. 893-894 (1967).
- [7] D. A. Cameron and E. N. Pugh, Jr., *Nature*, **353**, 161-164 (1991).
- [8] M. P. Rowe, N. Engheta, S. S. Easter, Jr., and E. N. Pugh, Jr., *J. Opt. Soc. Am. A*, **11**, 55-70 (1994).
- [9] G. P. Können, *Polarized Light in Nature*, Cambridge University Press, London (1985).
- [10] W. Saidel, J. Y. Lettvin, and E. F. MacNichol, Jr., *Nature*, **304**, 534-536 (1983).

Figure Captions

Fig. 1. Top panel depicts the top view of the experimental setup. A: Polarization analyzer; TNLC: twisted nematic liquid crystal; F: narrow-band filter. Bottom panel shows the front view of the tank (drawn to scale) with inside dimensions 30 cm x 30 cm x 15 cm. This tank is filled with water to which milk is added. The target is suspended in the middle of the tank.

Fig. 2. Application of the PDI system to an aluminum target suspended in diluted milk as illustrated in Fig. 1; 5 ml of ~~the~~^{whole} milk was added. A and B present the images $I_{||}(x,y)$ and $I_{\perp}(x,y)$ convolved digitally with a two-dimensional low-pass spatial filter. This filter is roughly a truncated gaussian, with maximal linear extent about 5 pixel widths; the images of the abraded patches are $\sim 80 \times 92$ pixels. The filter removes a periodic high spatial frequency artifact produced by the imaging system. Image intensities (ordinates) are expressed in the units of the 8-bit display, i.e., vary from 0 to $255 = 2^8 - 1$. C and D present $psI(x,y)/2$ and $pdI(x,y)+128$, respectively. (cf. Eqs. 1(a) and 1(b)); an offset of 128 was used, since most pixel values of $pdI(x,y)$ are near zero, and can be either positive or negative. E and F re-present the data of C and D, scaled with affine transformations that take advantage of the full display range. The transformed values are given by $psI(x,y)_{trans} = \alpha_{ps}[psI(x,y) - psI(x,y)_{min}]$ and by $pdI(x,y)_{trans} = \alpha_{pd}[pdI(x,y) - pdI(x,y)_{min}]$ where $\alpha_{ps} = 255/[psI(x,y)_{max} - psI(x,y)_{min}]$, and similarly for α_{pd} . In E, $psI(x,y)_{max}$ and $psI(x,y)_{min}$ were obtained from the disk region only; the resultant scale factor, $\alpha_{ps} \approx 6.4$, is such that the intensity variation of the disk region occupies the full display range. In F, $pdI(x,y)_{max}$ and $pdI(x,y)_{min}$ were obtained from the entire image, yielding $\alpha_{pd} \approx 38.4$. Abraded patches, not visible in Panels A, B, C, and D, are clearly visible in Panel F, but barely visible in Panel E. The vertical bands of pixels between the arrows at the right side of the images in A – F were averaged over y to generate numerical plots (as a function of x) shown in panels A' – F'.

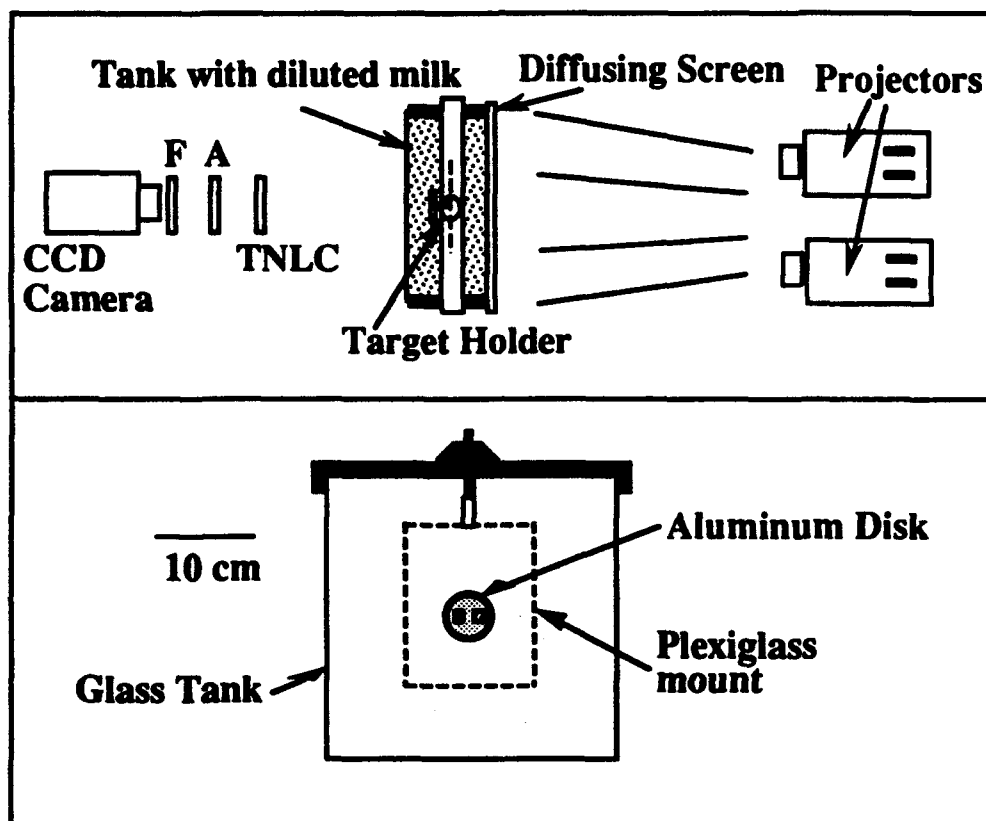


FIGURE 1

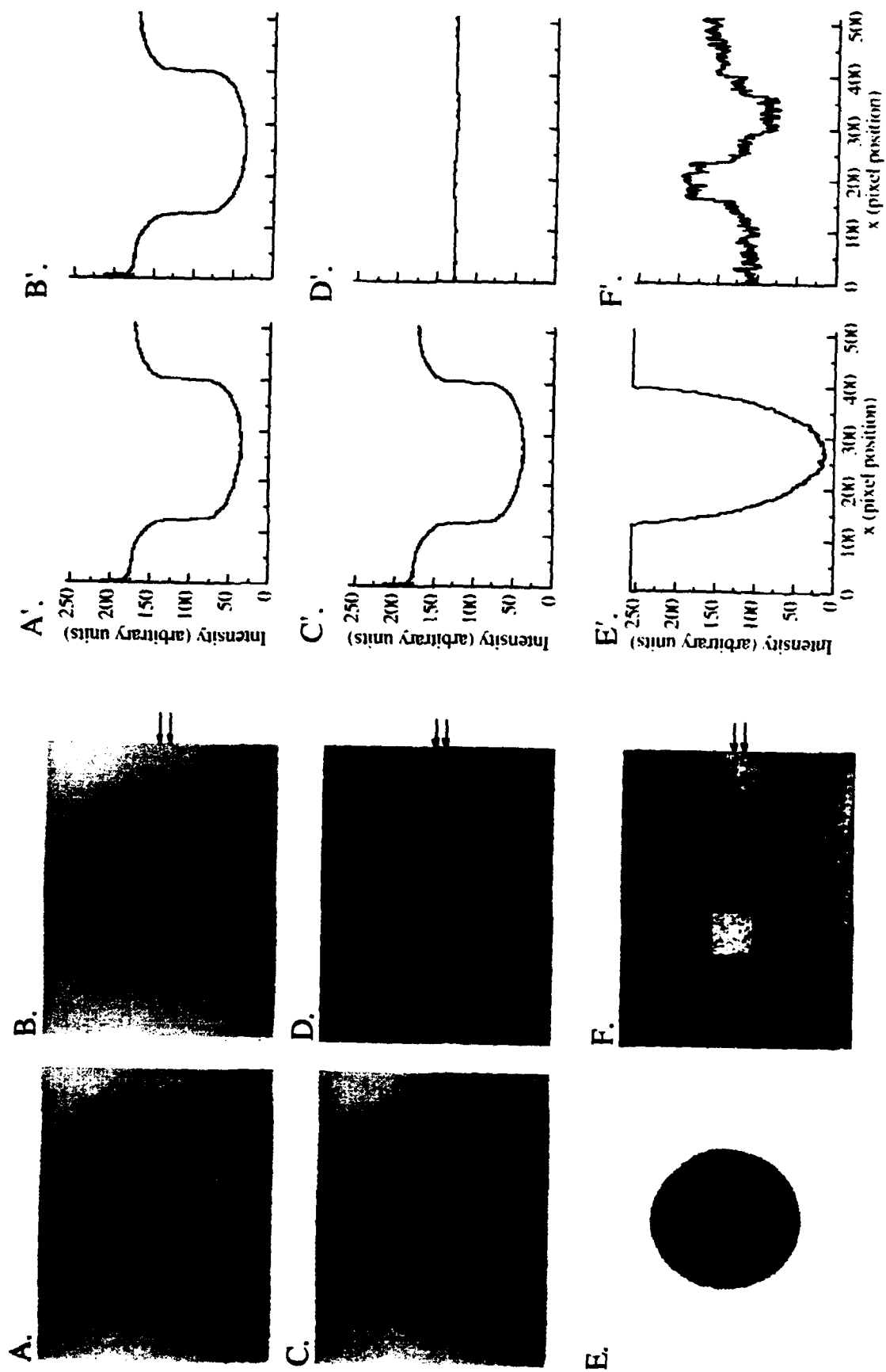


Figure 2.

APPENDIX B

Reprint of the Manuscript entitled

GRADED INDEX MODEL OF FISH DOUBLE CONE EXHIBITS DIFFERENTIAL POLARIZATION SENSITIVITY

Authors: M. P. Rowe, N. Engheta, S. S. Easter, Jr., and E. N. Pugh, Jr.

published in

Journal of Optical Society of America A
Vol. 11, No. 1, pp. 55-70, January 1994.

Graded-index model of a fish double cone exhibits differential polarization sensitivity

M. P. Rowe

Institute of Neurological Sciences, University of Pennsylvania, Philadelphia, Pennsylvania 19104

N. Engheta

The Moore School of Electrical Engineering, University of Pennsylvania, Philadelphia, Pennsylvania 19104

S. S. Easter, Jr.

Department of Biology, University of Michigan, Ann Arbor, Michigan 48109

E. N. Pugh, Jr.

Department of Psychology, University of Pennsylvania, Philadelphia, Pennsylvania 19104

Received October 1, 1992; revised manuscript received June 28, 1993; accepted June 29, 1993

The close apposition of the inner segments of the two cones that combine to form a double cone causes the pair of cone inner segments to guide light as a unitary structure whose transverse sections are roughly elliptical. Electron micrographs of the photoreceptors of a green sunfish (*Lepomis cyanellus*) retina provide evidence that the refractive index in the ellipsoid region of the inner segments of the double cones is higher in the center than at the perimeter. The hypothesis that the shape and refractive-index gradient could confer differential polarization sensitivity on double cones is examined with a two-dimensional waveguide model of a double-cone inner segment. The model has a dielectric constant that varies parabolically along the narrowest (x) dimension, leading to the index profile: $n(x) = n_{\text{max}}[1 - (x/x_0)^2]^{1/2}$, where n_{max} is the peak value of the index and x_0 is a parameter specifying the rate at which the index decreases with increasing $|x|$. A quantity, the polarization contrast, is introduced as a measure of the differential polarization sensitivity of adjacent receptors in the square mosaic of double cones in the sunfish retina. Polarization contrast is proportional to the relative difference in power absorbed by two double cones oriented with their shortest axes orthogonal to each other and stimulated by a field of uniform polarization. Polarization contrast is computed as a function of wavelength for appropriate values of n_{max} and x_0 . For normally incident light polarized parallel to one of the two axes of the double cones' cross sections, the polarization contrast is generally between 1% and 5% for wavelengths ranging from 550 to 750 nm. Over most of those wavelengths the polarization contrast of the graded-index-model double cone is approximately five times as large as that of a homogeneous-slab model of the same size and average refractive index. Additional benefits of a graded index, optical isolation of adjacent photoreceptors and antireflection at the photoreceptor entrance, are also discussed.

1. INTRODUCTION

A. Vertebrates' Use of Polarization

Many vertebrates are capable of extracting information from the state of polarization of visible light,¹⁻⁴ but the physical mechanism underlying this ability is not yet established. In particular, the sensitivity of the green sunfish (*Lepomis cyanellus*) to small, linearly polarized targets has been reported to be a periodic function of polarization angle with 90° periodicity and modulation depth of as much as half a log unit.⁵ The action spectrum of this differential sensitivity corresponds to that expected for the pigment of the green sunfish's double cones ($\lambda_{\text{max}} = 621 \text{ nm}$).⁷ Double cones⁸ are cone pairs that are fused along the adjacent faces of their inner segments; they are found in the retinas of many fish, reptiles, and birds⁹ and at least one marsupial¹⁰ and one monotreme mammal.⁹ In this paper we examine the hypothesis that the shape (or, more specifically, the refractive-index profile) of the double cones of sunfish confers on those cones a differen-

tial polarization sensitivity. The next subsection provides the background for, and a further elaboration of, this hypothesis.

B. Double Cones As Unitary, Birefringent Waveguides

The index of refraction inside vertebrate photoreceptors is higher than the index of the intercellular medium surrounding them.¹¹ Because of this difference in refractive indices, photoreceptors behave as miniature fiber-optic cables,¹² guiding light from their inner segments into (and through) their outer segments, where phototransduction occurs. Figure 1 shows a radial section of the photoreceptor layer of a green sunfish retina and illustrates a double cone in longitudinal section; the lower part of the section (dashed line marked b) is $\sim 3 \mu\text{m}$ beyond the external limiting membrane. Figure 2 shows a series of transverse sections, taken at the levels marked by the respective lowercase letters in Fig. 1. Figures 1 and 2 illustrate that the two cones that combine to form a double cone are in direct contact with each other from the external limiting



Fig. 1. Electron micrograph of the photoreceptor layer of a green sunfish. The sunfish was anesthetized by immersion in a 0.2% solution of tricaine methanesulfonate (Sigma). After breathing had stopped, the heart was perfused with a 1% solution of sodium nitrite in 0.05-M sodium cacodylate buffer to expel blood cells from the circulatory system; this was followed by perfusion with a similarly buffered solution of 3% glutaraldehyde. The eyes were removed from the fish; the lens, iris, and cornea were removed; and the eye cups were stored overnight in fresh fixative. The eye cups were rinsed, dehydrated, and stained in block overnight with 2% uranyl acetate in 0.05-M maleate buffer. They were then dehydrated through a graded series of alcohol and embedded in epon. Semithin sections (1–2 μm thick) were stained with Toluidine Blue and examined light microscopically. Ultrathin sections (0.1 μm thick) were cut, mounted on formvar film-coated one-hole copper grids, stained with lead citrate, and viewed in a Philips 300 electron microscope. The plane of section is perpendicular to the surface of the retina: parallel to the long axis of the photoreceptors. Light enters from below (the vitreal direction). The photoreceptor nuclei lie below the field of view. The dashed lines indicate the levels at which the sections shown in Figs. 2b–2f were cut. The central paired structure with the long outer segments, os, is the double cone, flanked on the right by another double cone and on the left by a single cone. The subcellular components are identified in Fig. 2.

membrane to the bases of the two outer segments. Because the inner segments of the two members of a double cone are in such close apposition, the composite structure (i.e., the double-cone inner segment) can be expected to act as a single waveguide. Evidence for energy coupling between the two component cones of a goldfish (*Carassius auratus*) double cone has been reported by Tobey et al.¹³

In many animals with double cones the inner segments of the double cones have roughly elliptical cross sections in planes perpendicular to the guiding axis. That the cross sections of the double cones of the green sunfish are roughly elliptical can be seen from Figs. 2 and 3. We hypothesize that their noncircular cross sections and material-density profiles cause double cones to exhibit geometric birefringence such that waves linearly polarized parallel to the long axis of the inner segment cross

section are more effectively guided than waves polarized parallel to the short axis, that is, light polarized along the long axis has a greater ability to stimulate phototransduction.¹⁴ Such geometric birefringence could allow the double cones to act as miniature, although imperfect, polarization analyzers: for a given incident intensity, the fraction of power guided into the photoreceptor outer segments could be a function of the linear polarization state of the incident beam.

Aside from depicting the shape of the double cones' cross sections, Figs. 2 and 3 show that the double cones of the sunfish are locally arranged in a roughly square mosaic,¹⁵ an arrangement shared by many teleosts^{16,17} and at least one bird.¹⁸ In this mosaic the long axes of the double cones' cross sections form the sides of the squares. If the hypothesis that double cones are geometrically birefringent waveguides is correct, then the two orientation classes of double cones in the square-pattern mosaic are equivalently two polarization classes of photoreceptor. Bernard and Wehner have shown that polarization vision can be understood in many ways by analogy to color vision.¹⁹ In this analogy two orientation classes of double cones in a polarization-sensitive animal would correspond to two chromatic classes of single cones whose pigments are maximally sensitive to different wavelengths in a color-sensitive animal. We propose that the two orientation classes of double cone in the green sunfish are ideally situated to function as the input for the computation of a retinal polarization-difference image, much as the photoreceptors of, for example, the primate fovea provide the basis for the computation of a chromatic-difference image.²⁰ The significance of this sensory cell arrangement will be discussed below, where it will be clear that the magnitude of the differential polarization sensitivity of the animal need not be explained by an equivalent magnitude of differential sensitivity in the individual receptors.

To recapitulate, in this section we have outlined the double-cone-mosaic hypothesis of polarization vision, a hypothesis that comprises two propositions: (1) the double-cone inner segment functions as a weak polarization analyzer by virtue of geometric birefringence, and (2) the mosaic of double cones serves as the input to a neural differencing network that computes a local polarization difference at each point in the animal's retina. Our focus in this investigation is on proposition (1).

2. GRADED-INDEX MODEL OF THE SUNFISH DOUBLE-CONE INNER SEGMENT

A. Anatomical Evidence That Double Cones are Waveguides with an Inhomogeneous Core

Figures 1 and 2b–2e show that, as in other vertebrates,¹¹ the sunfish's photoreceptor inner segments have a specific region that is densely packed with mitochondria. Photoreceptor mitochondria are well known for their essential role in metabolism and are well positioned to serve the high energy demands of the photoreceptor dark-current and phototransduction cascade. However, the concentration of mitochondria in vertebrate photoreceptors also serves to increase the photoreceptors' refractive index, enhancing the inner segments' ability to guide light.¹² We now concentrate our attention on the mitochondria because of their role in the establishment of waveguiding in

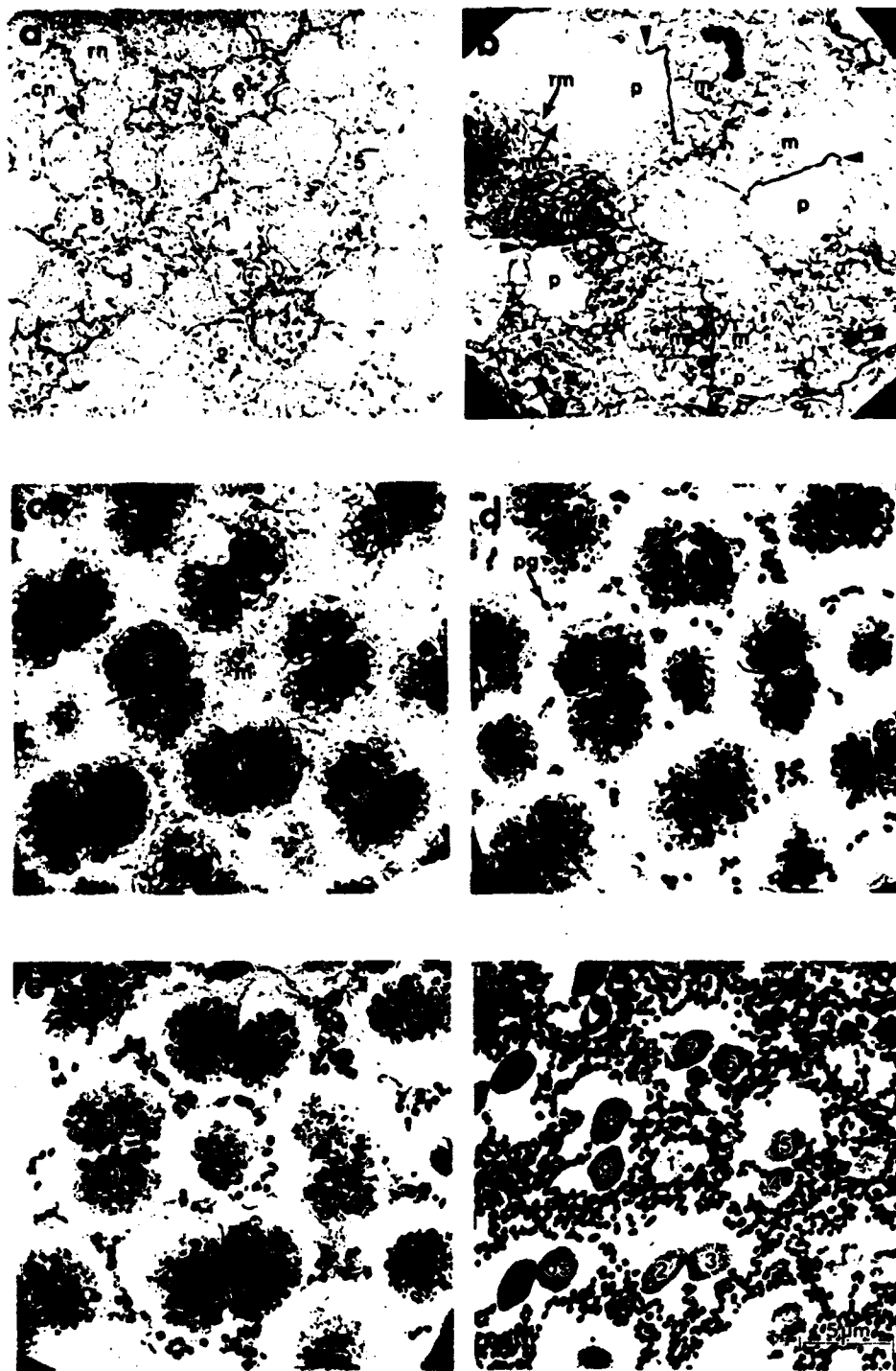


Fig. 2. Six electron micrographs at different levels through the same tetrad of cones, all at the same magnification and orientation. The preparation of the tissue was the same as that for Fig. 1. The plane of section is the same in all panels: parallel to the retinal surface and perpendicular to the long axis of the photoreceptors; the approximate levels of panels b-f are shown in Fig. 1. **a:** This section passes through the photoreceptor nuclei (at a level below the field shown in Fig. 1). The rod nuclei, rn, are finely granular; the cone nuclei, cn, are more mottled. The nine cones that form one square of the double-cone mosaic are indicated by the numbers 1-9, and some or all of these cones are numbered in other panels as well. **b:** This section passes through the base of the cone inner segments; the parabolid, p, and the mitochondrial cluster, m, are indicated in the four double cones. They are surrounded by the fine processes of the Müller cells, mc, and the rod myoids, rm, the attenuated processes that connect the rod nuclei to their inner segments. The arrowheads indicate the dark intercellular junction between the two members of the double cones. **c:** At this more-distal level the cone inner segments occupy essentially the entire cross section of the retina, and the cross section of the interior of the double cone is nearly filled by the mitochondrial cluster. The electron density of the mitochondrial cluster is greater than in b, and the gradients of electron density across the double cones are evident. **d:** At this level of section the cones fill most of the retinal cross section, but pigment granules, pg, from the pigmented epithelium begin to intrude from above. Within each double cone the mitochondrial cluster occupies a smaller fraction of the cross section than in c, reflecting the taper evident in Fig. 1. The gradient in electron density is still evident. **e:** The mitochondrial clusters have tapered still more, the pigment granules are more numerous, and the extracellular space around the cones has increased relative to that shown in d. **f:** The cone outer segments, os, occupy a much smaller fraction of the retinal cross section; the pigmented processes, a much larger one.

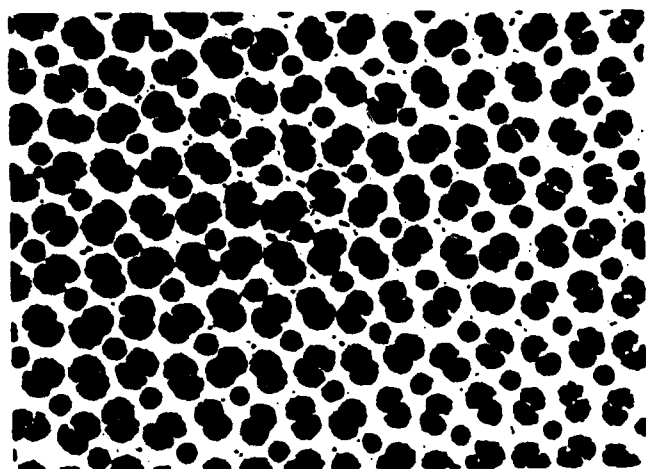


Fig. 3. Semithin sections prepared as described in the caption of Fig. 1 and viewed with a light microscope. This figure demonstrates the regularity in the photoreceptor mosaic of the green sunfish. The regularity seen here is representative of the mosaic across the entire retina (see Ref. 15).

photoreceptors. Figures 1 and 2 illustrate three features that we believe are of fundamental importance for understanding the mitochondria's influence on the waveguiding behavior of double-cone inner segments.

Mitochondria concentrated near the double-cone center. First, the distribution of mitochondria in each of the two cones that unite to form a double cone is concentrated near the common boundary of the two (i.e., along the fusion boundary). This asymmetrical packing of mitochondria in the individual cones that combine to form a double cone stands in sharp contrast to the distribution of mitochondria in the single cones seen at the center of each square of the mosaic in Fig. 2. In the single cones the mitochondrial cluster is centered in the cytoplasm at a more-or-less-uniform distance from the cytoplasmic membrane.

Elliptical annulus of cytoplasm surrounding mitochondria. A second feature of the distribution of mitochondria that we believe to be a determinant of the waveguiding behavior of the double-cone inner segments is that the region containing mitochondria is surrounded by an annulus of cytoplasm devoid of mitochondria. Thus the mitochondrial region is contained within a reasonably well-defined boundary that has the same shape as the outer envelope of the double cone but is clearly interior to that outer boundary. Interestingly, there is one perspective from which the distribution of mitochondria in the double cone resembles that in the single cone: each has an annulus of cytoplasm circumscribing the mitochondrial region. In the case of the double cone, however, the annulus of cytoplasm follows the perimeter of the composite structure rather than the perimeter of the individual member cones. That is, the distribution of mitochondria within a single cone resembles the distribution of mitochondria in a double cone as a composite structure and not the distribution of mitochondria in an individual member of a double-cone pair.

In the anatomical literature the mitochondrial region of the inner segment of single photoreceptors is known as the ellipsoid. This name refers to the structure's three-dimensional shape in single cones.²¹ We can summarize our first two observations by saying that the double-cone

inner segment, while comprising two distinct photoreceptors, appears from the optical perspective to have a single ellipsoid. That is, the mitochondrial distribution in the double-cone inner segment forms a single functional body that we may call "the double-cone ellipsoid." We consider the existence of the unitary double-cone ellipsoid to be an adaptation that functions to unify the member inner segments of a double cone into a single waveguide.

Greater electron density near the centers of ellipsoid cross sections. The third characteristic feature of the mitochondrial distribution in double-cone inner segments is that the mitochondria nearest the center of transverse sections of the ellipsoid are more electron dense than the mitochondria near the ellipsoid's perimeter. Figures 2c-2e show a clear gradient in electron density across the mitochondrial cluster in each double cone. This gradient in electron density cannot represent a differential packing of mitochondria along the z axis (into and out of the micrographs), because these sections are only $0.1 \mu\text{m}$ thick, much less than the thickness of a typical mitochondrion. Thus the gradient is in the form of a differentiation among mitochondria: the mitochondria toward the center of the cell are more electron dense than those at the periphery.

It seems unlikely to us that the observed differential electron density of mitochondria is an artifact of the penetration of the fixatives and stains used to prepare the tissue (as described in the caption of Fig. 1). In the case of a penetration artifact, we would expect the staining to be a simple decreasing function of the distance to the nearest point on the plasma membrane. However, the micrographs show that this is not the case: the electron density of the mitochondria is an increasing function of the mitochondrion's distance from the cell membrane. Moreover, at the scleral end (near the outer segments) the mitochondria are darker than at the vitreal end (near the nucleus) even in the regions immediately adjacent to the cytoplasmic envelope (see Fig. 1). Thus whatever process determines the observed electron density of individual mitochondria apparently operates differentially in all three dimensions. The variation in mitochondria as a function of position in the inner segment is not unique to sunfish. It is well established that photoreceptor mitochondria are often modified, relative to the mitochondria in other cells, in ways that affect the optical properties of the photoreceptor, and these modifications are more prominent around the perimeter and the scleral end of the ellipsoid.²²⁻²⁵

The differential electron density of the mitochondrial regions in the sections shown in Fig. 2 must represent an increase in the concentration of either an electron-dense substance or a substance for which the fixative or stains have an affinity. The osmium tetroxide used in these preparations binds principally to lipids, the uranyl acetate binds to nucleic acids, and the lead citrate binds to both osmium and uranium atoms. If the variation in electron density arises from a differential affinity for the stain, it will still indicate a correlated variation in the concentration of lipid or nucleic acids in the unstained tissue. An increase in the concentration of nucleic acids or lipids results in an increase in refractive index.²⁶

In summary, analysis of electron micrographs supports the general hypothesis that the refractive index of the ellipsoid region of sunfish double cones is highest in

the center of the cross section and declines toward the perimeter.

B. Mathematical Analysis of the Double-Cone Inner Segment's Waveguiding Properties

While our anatomical observations support the proposition that the double-cone inner segment is a unitary graded-index waveguide with a noncircular cross section, alone they do not provide sufficient quantitative constraints for analyzing the properties of the guide. In this section we synthesize our anatomical observations with additional information and hypotheses into a mathematical model suitable for examining the waveguiding behavior of the double cone.

From the outset we acknowledge that we have made several simplifying assumptions in constructing the model. One of the crudest of these is that our model neglects variation in properties along the longitudinal (z) axis. We justify our neglect of z -axis variation at this time by the need for a relatively simple, tractable model. Nonetheless, the anatomical data that we have presented show clear and systematic variation along the z axis that may play an important role in the waveguiding behavior of the double cone. We take up this matter again in Section 4.

In addition, in order to investigate quantitatively the waveguiding properties of the double cones, we have made specific assumptions about the shape and height of the refractive-index profile. Constraints on these assumptions arise from measurements of the size of the double cones, from previous estimates of the average refractive index of the ellipsoids of photoreceptors, and from the maximum value that the refractive index can attain in a living cell.

Size of the waveguide cross section. From the electron micrographs of Figs. 1 and 2 it is clear that the size of the double-cone cross section varies somewhat with position along the z axis. Nonetheless, as noted above, we have chosen to neglect z -axis variations and have selected a single (x - y) cross section of a double cone as representative. In order to generate a conservative estimate of the polarization properties of the double cone, we based our model on the largest cross sections that have been measured in living double cones. The dehydration that is a necessary step in the preparation of the retina for viewing the tissue with an electron microscope causes the cells to shrink somewhat. Because of this shrinkage, it is better to estimate the size of the cones by viewing them with a light microscope under more-natural conditions. Light-microscopic observations of fixed and stained retinas or of fresh cones suspended in fish Ringer's solution indicate that a reasonable upper limit to the largest cross sections of sunfish double-cone inner segments is $7\ \mu\text{m} \times 14\ \mu\text{m}$.¹⁵

Average refractive index. Using refractometry and differential interference contrast microscopy, Sidman studied the photoreceptors of many animals.¹¹ His measurements showed that the ellipsoid region of cone inner segments have an average refractive index of approximately 1.39. Although he did not investigate green sunfish in his study, he did examine photoreceptors of a wide array of vertebrates including frog, rat, chicken, and monkey. Initially we adopt the value 1.39 as the average refractive index across the double-cone inner segment.

Refractive-index profile. On the basis of the anatomi-

cal evidence presented above, we conclude that the refractive index of the double-cone inner segment is highest in the center of the structure and declines monotonically to the perimeter. However, the anatomical data cannot be converted into a specific formula for the refractive-index profile, because there is no established relationship between the electron density in a fixed and stained retina and the electron density in living photoreceptors. Figure 4 illustrates how our choice of refractive-index profile is motivated by, and consistent with, our anatomical observations. Figure 4A is a magnified view of cones 8 and 9 from Fig. 2c. Figure 4B is a contour plot of the digitally filtered density of the negative used to generate Fig. 4A (see Fig. 4 caption for details). We embed the contour plot in a slab waveguide to indicate the coordinate system used throughout this paper. Figure 4C shows three lines of the digitally filtered data taken from the locations indicated by the lines in Fig. 4A. The mesh plot in Fig. 4D provides a different view of the data presented in the contour plot of Fig. 4B. Figures 4C and 4D include a curve that matches the index profile that we will be using in our model. We began by approximating the variation of the dielectric constant as a two-dimensional parabolic gradient:

$$\epsilon(x, y) = \epsilon_{\text{max}}[1 - (x/x_0)^2 - (y/y_0)^2]. \quad (1)$$

The dielectric constant is proportional to the square of the refractive index, so Eq. (1) leads to

$$n(x, y) = n_{\text{max}}[1 - (x/x_0)^2 - (y/y_0)^2]^{1/2}. \quad (2)$$

The index variation of Eq. (2) is consistent with our anatomical data and has some precedent in the literature.^{27,28} Equations (1) and (2) are assumed valid for the intracellular region of the photoreceptors, which can be approximated by the region in which $[x/(d/2)]^2 + (y/d)^2 \leq 1$, where d is the length of the minor axis of the model double cone's cross section. The constants ϵ_{max} and n_{max} are the values of the dielectric constant and the refractive index at the center of the guide. The constants x_0 and y_0 determine how rapidly the dielectric constant and the refractive index drop with distance away from the origin along the x and the y axes, respectively. The parameters x_0 and y_0 can also be expressed in terms of the above parameters d and n_{max} : $y_0 = 2x_0 = d[\sqrt{1 - (n_{\text{cl}}/n_{\text{max}})^2}]^{-1/2}$, where n_{cl} is the index of the extracellular fluid. With $d = 7\ \mu\text{m}$, $n_{\text{cl}} = 1.33$, and with Sidman's value of 1.39 for the average value of the refractive index across the inner segment at the ellipsoid region,¹¹ the values of the parameters n_{max} , x_0 , and y_0 are determined and readily computed: $n_{\text{max}} = 1.42$, $x_0 = 10.0\ \mu\text{m}$ and $y_0 = 20.0\ \mu\text{m}$.

In constructing the model we made one further approximation. We chose to neglect the variation in refractive index along the y axis, so that the assumed index profile of our model is one dimensional:

$$n(x) = n_{\text{max}}[1 - (x/x_0)^2]^{1/2} \quad (3)$$

The neglect of y -axis variation considerably simplifies the calculations and is not unreasonable given that the variation along the x axis dominates the behavior of the guide.²⁹

Bound-mode solutions of the model waveguide. To solve for the modes of our model double cone, we used the infinite parabolic profile. This model, where Eq. (3) is

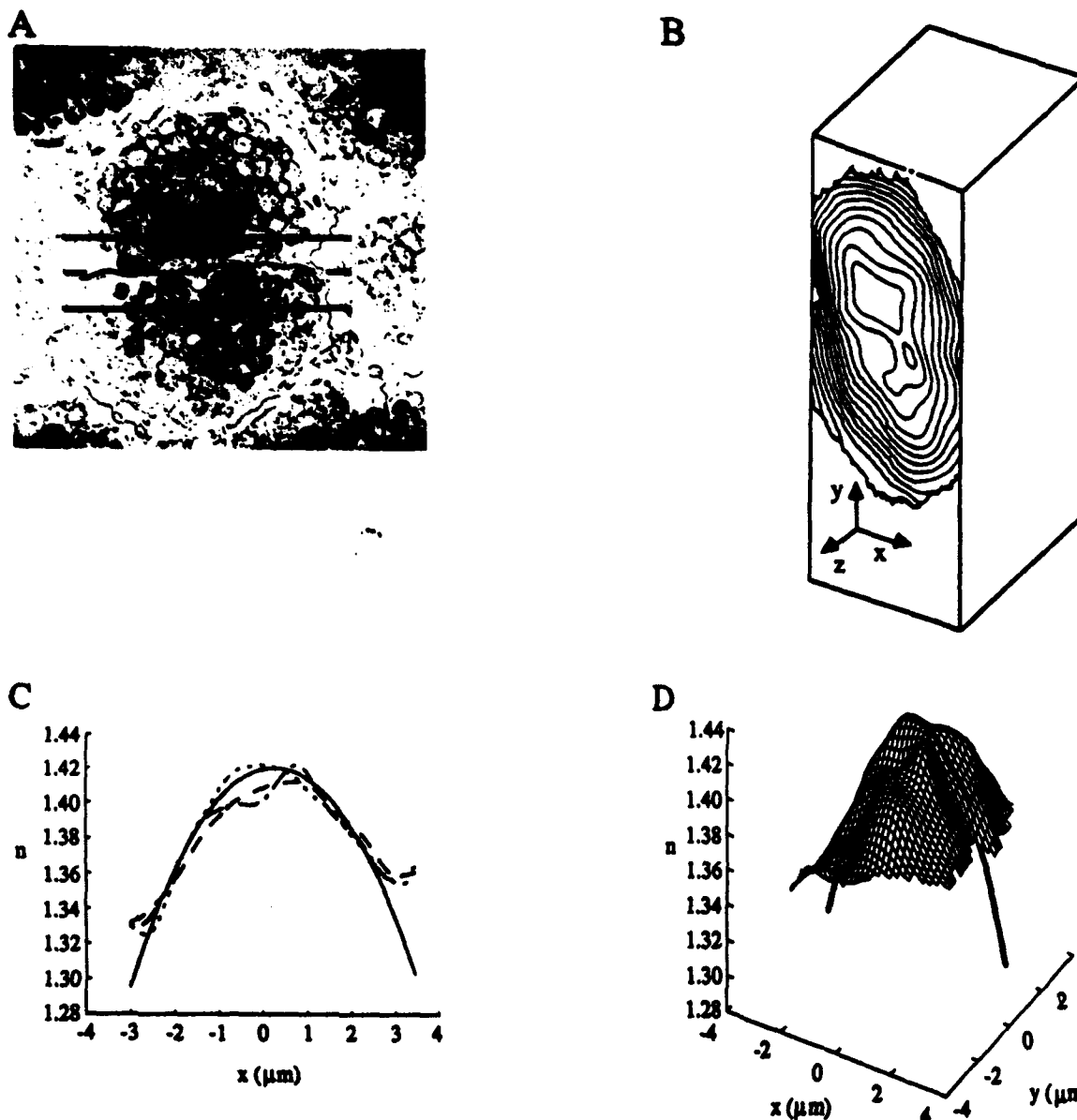


Fig. 4. Relationship between the anatomy and the mathematical model. A, A reproduction of one of the double cones (8–9) from the section shown in Fig. 2c. The scale bar at the upper left of the cell is 620 nm long; however, it must be remembered that this tissue has been shrunk somewhat by its preparation. The other lines refer to C, below. B, The negative that generated A was photographed against a backlit piece of white acrylic by a Hamamatsu CCD camera whose output went to an Imaging Technologies Series 151 image-analysis system. After we had calibrated the camera/image-analysis system to ensure linearity of the output over intensity and space, we used the series 151 to digitize the image of the negative as acquired by the CCD camera. The digital image data was then loaded into the MATLAB computer program (version 4.0, the MathWorks, Inc.). In MATLAB the electron-density data was convolved with a Gaussian filter that appropriately averaged the data to convert the density profile to an approximation of the index profile. The filter fell in value to 10% of its maximum at 620 nm from the center and was normalized by its integral over all x and y being set to 1. The filtered image data were then masked so that only the region within the cytoplasm was displayed, and a contour plot was generated. The contour plot is viewed at an angle and truncated to fit into a slab indicating the coordinate system used in the model. Note that the contour lines follow the general outline of the composite structure: that optically the boundary between the ellipsoid of cell 8 and the ellipsoid of cell 9 is essentially nonexistent. C, Three lines from the filtered image, data were scaled to suggest the form of the refractive-index gradient. We accomplished scaling by first setting the index of the extracellular regions to 1.33 and then setting the average density across the x axis near the center of the cell to 1.39. The three lines that we scanned to generate this plot are indicated in A. The dotted curve came from the top line in A, and the dotted-dashed curve came from the center line of A (only the ends are drawn, so as not to obscure the details of the figure). The dashed curve is the bottom line in A. The solid curve is a least-squares fit of the data from the top line in A (the dotted curve of C). The solid curve satisfies Eq. (3) with $n_{\text{max}} = 1.42$ and $x_0 = 8 \mu\text{m}$ (leading to $d = 5.6 \mu\text{m}$). We stress that the numbers along the ordinate are crude approximations that do not derive from direct measurements of the refractive index. D, Mesh plot of the data displayed in B. The solid curve used to fit the data in C is drawn at 10 times the thickness of the grid lines of the mesh.

valid for all x , has the virtue that the bound-mode solutions of the vector wave equation derived from Maxwell's equations and Eq. (3) are in analytical closed form for incident radiation polarized along the y axis. Moreover, with

one more approximation (presented below), there exists an analytical solution for the bound modes excited by radiation polarized along the x axis, as well. The solution of the equations for the guided modes excited by light polar-

ized along the y axis yields the TE modes,³⁰ which have electric fields of the form

$$E_{x,m}(\delta) = A_{TE,m} H_m(\delta) \exp(-\delta^2/2), \quad (4)$$

where $\delta = (k_0/x_0)^{1/2}x$, k_0 is the free-space wave number, $A_{TE,m}$ is a parameter used to normalize modes such that each carries unit power per unit length of the y axis, and $H_m(\delta)$ is the Hermite polynomial of order m ($m = 0, 1, 2, \dots$).³¹

Since we will be assuming a monochromatic incident field with angular frequency ω , and since we are ignoring the variations in size and index along the z axis, all fields of interest will be waves whose z and t dependence is expressed in the factor $\exp[i(\omega t - \beta_{TE,m}z)]$. It can be shown³¹ that $\beta_{TE,m}$ must satisfy

$$\beta_{TE,m}^2 = (k_0 n_{\max})^2 - \frac{(2m+1)k_0 n_{\max}}{x_0}. \quad (5)$$

In the second-order differential equation that must be satisfied for an electromagnetic wave propagating along the z axis and polarized along the x axis (the TM modes), we can discard the terms of order x^4/x_0^4 ; those terms would change the coefficient of the electric field in this equation by at most 0.0023% for $n_{\max} = 1.42$ and $x_0 = 10.0 \mu\text{m}$. The solutions to the equation without those terms are of the form

$$E_{x,m}(\rho) = \frac{A_{TM,m}}{n(x)} H_m(\rho) \exp\left(\frac{-\rho^2}{2}\right), \quad (6)$$

where $\rho = x[(k_0 n_{\max}/x_0)^2 + 4/x_0^4]^{1/4}$ and $A_{TM,m}$ is a normalization parameter analogous to $A_{TE,m}$.

In the TM case there is a small longitudinal component of the electric field that can be found from the transverse component with the equation

$$E_{z,m}(x) = \frac{-i}{\beta_{TM,m}} \left\{ \frac{d[E_{x,m}(x)]}{dx} - \frac{2xE_{x,m}(x)}{(x_0^2 - x^2)} \right\}, \quad (7)$$

where $\beta_{TM,m}$ is determined by

$$\beta_{TM,m}^2 = (k_0 n_{\max})^2 - \frac{1}{x_0^2} - (2m+1) \left[\left(\frac{k_0 n_{\max}}{x_0} \right)^2 + \frac{4}{x_0^4} \right]^{1/2}. \quad (8)$$

As indicated above, the fields described by Eqs. (4)–(8) are exact (within the approximation for the TM modes) only if Eq. (3) is valid for all x . However, they represent a good approximation to the fields bounded by a guide described by Eq. (3) valid for the region inside the double cone if all the field components [e.g., from Eqs. (4), (6), and (7)] die off quickly before reaching the region over which Eq. (3) is no longer valid. In order to use the solutions represented by Eqs. (4)–(8), we adopted the criterion that a mode be considered bound only if its effective index was greater than 1.33.³² A physical intuition of the significance of this restriction can be obtained from the WKB approximation. In that analysis, bound waves are reflected back toward the center of the guide at the point where the refractive index is equal to the effective index. Our restriction is equivalent to one in which a mode is considered guided only if the so-called walls of the guide are inside the

perimeter of our model double cone. Figure 5 shows the form of all the even-symmetric modes that meet this criterion when $n_{\max} = 1.42$ and $x_0 = 10.0 \mu\text{m}$. The value of x_0 determined in the caption for Fig. 4 is smaller than $10.0 \mu\text{m}$, but, as discussed above, we begin our analysis with a limiting case. In Fig. 5 we show only even-symmetric modes, because given the incident radiation that we assume below, these are the only modes that will be excited. Note the magnitudes of the fields where $x = d/2$.

Calculation of the power extracted from different input polarizations. We now examine the power extracted by our model photoreceptor when it is excited by a uniformly polarized, normally incident plane wave.³³ We assumed that, before the entrance of the waveguide, the index is homogeneous and equal to that of the extracellular fluid. The change in refractive index at the interface leads to a reflection, which we modeled by calculating the Fresnel transmission coefficient at each point along the cross section.³⁴ We then multiplied the amplitude of the incident plane wave by the resulting function of x . Use of the Fresnel coefficients is, of course, another approximation, but its simplicity makes its usage common.³⁵ The guided field can then be determined by expansion of the transmitted field into the modes described by Eqs. (4), (6), and (7), since the modes form an orthogonal set over the infinite cross section. That is, the electric field of any guided wave can be expressed as the sum of these modal solutions:

$$E_{\text{guided}} = \sum_m \text{Re}\{p_{TM,m} E_{x,m}(x) \exp[i(\omega t - \beta_{TM,m}z + \phi_{TM,m})]\} \hat{x} \\ + \text{Re}\{p_{TE,m} E_{x,m}(x) \exp[i(\omega t - \beta_{TE,m}z + \phi_{TE,m})]\} \hat{y} \\ + \text{Re}\{p_{TM,m} E_{z,m}(x) \\ \times \exp[i(\omega t - \beta_{TM,m}z + \phi_{TM,m} - \pi/2)]\} \hat{z}, \quad (9)$$

where Re means the real part of, \hat{x} , \hat{y} , and \hat{z} are unit vectors along the x , y , and z axes, respectively, the p 's are amplitude coefficients, the ϕ 's are relative phases of the modal fields, and all other terms are as defined above.

The polarization of any normally incident wave can be resolved into two waves polarized along the x and y axes, so it is sufficient to analyze the propagation of the fields resulting from incident waves at these two polarizations only. Furthermore, since a normally incident plane wave has even symmetry around the plane defined by $x = 0$, we can determine by inspection that the wave will excite only even-indexed modes.

We thus obtain five bound even modes for each of the two incident polarizations. The relative contribution of each of the modes was determined by numerical integration with software written by us in C, and also with MATHEMATICA (version 1.2, Wolfram Research, Inc.). These values can be found in Table 1. In order to determine what these numbers mean in terms of excitation of the double cones, we calculated the fraction of propagated energy that would be available for driving phototransduction (i.e., chromophore isomerization). We will continue to use the modes determined from the lossless parabolic profile model, although we recognize that for the outer segments, basically a pair of tapering circular cylinders, this approximation is somewhat coarse. The analysis will at least provide a reasonable approximation to the fields present at the entrance to the outer segments, because

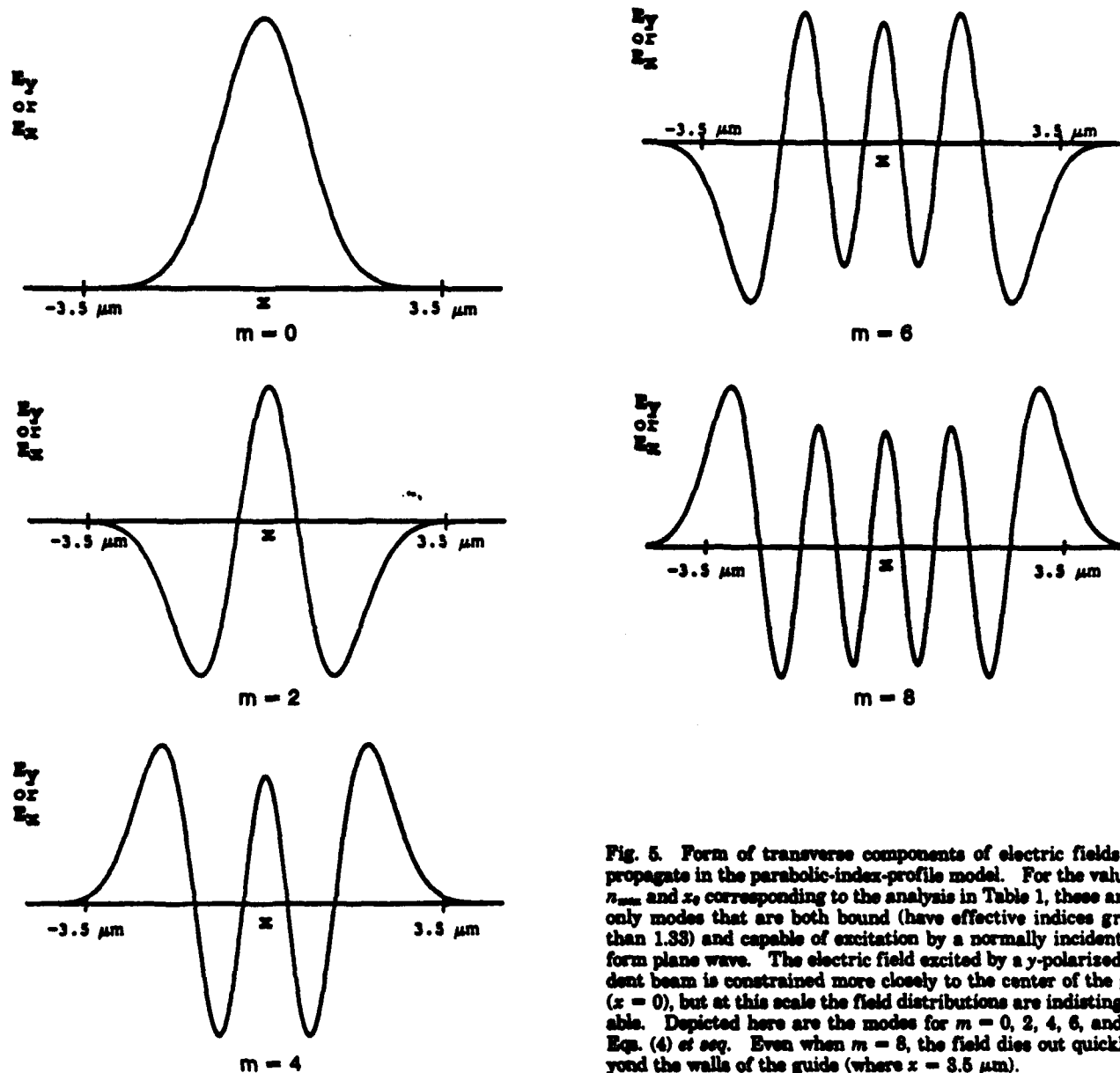


Fig. 5. Form of transverse components of electric fields that propagate in the parabolic-index-profile model. For the values of n_{max} and x_0 corresponding to the analysis in Table 1, these are the only modes that are both bound (have effective indices greater than 1.33) and capable of excitation by a normally incident uniform plane wave. The electric field excited by a y-polarized incident beam is constrained more closely to the center of the guide ($x = 0$), but at this scale the field distributions are indistinguishable. Depicted here are the modes for $m = 0, 2, 4, 6$, and 8 in Eqs. (4) et seq. Even when $m = 8$, the field dies out quickly beyond the walls of the guide (where $x = 3.5 \mu\text{m}$).

Table 1. Coefficients Obtained from Analysis of the Graded-Index Model*

Coefficient	Mode Number				
	0	2	4	6	8
A_{TE} (V/m)	13420	4778	694.7	63.89	4.302
A_{TM} (V/m)	18980	6663	954.7	86.50	5.735
β_{TE} (μm^{-1})	14.3347	14.1329	13.9283	13.7206	13.5097
β_{TM} (μm^{-1})	14.3343	14.1326	13.9279	13.7202	13.5092
p_{TE}	0.0028	0.0020	0.0017	0.00157	0.0015
p_{TM}	0.0028	0.0020	0.0017	0.00157	0.0015
$a_{m\parallel}$ (μm^2)	38.48	19.52	14.86	12.52	10.63
$a_{m\perp}$ (μm^2)	38.39	19.30	14.54	12.12	10.16

*This table represents the coefficients for a waveguide whose index-of-refraction profile is satisfied by Eq. (3), with $x_0 = 10.0 \mu\text{m}$ and $n_{\text{max}} = 1.42$. All the numbers in this table correspond to the modes associated with an incident field whose wavelength is 630 nm in free space. The A 's are coefficients that are established to orthonormalize the modes; with these coefficients each mode carries unit power per unit length of the y axis. The β 's are the propagation constants, or longitudinal wave numbers. The p 's are expansion coefficients that are obtained when a normally incident uniform plane wave is expanded into the bound orthonormal modes; the TE and TM modes are excited when the incident wave is polarized along the y axis and the x axis, respectively. The a 's are defined by Eqs. (10) and (11), with $P_{\text{inc}} = 1 \text{ W/m}^2$. Subtracting the corresponding a 's and dividing by the average of the power received from each of the incident polarizations, one obtains C_{pm} as defined by Eq. (12). For this case the value is 1.6%.

the actual fields should be similar to our model fields in the ellipsoids, and the ellipsoids directly about the bases of the outer segments. As can be seen from Fig. 1, the perimeters of the outer segment and the ellipsoid are contiguous.

The absorption of light by a photopigment is proportional to the square of the scalar product of the electric-field vector and the transition-moment vector of the absorbing chromophore.³⁸ For the TE modes we need concern ourselves only with the square of the electric field, because the pigments are free to rotate in the disks of the photoreceptor outer segments,^{37,38} and thus, on average over time, all orientations of the chromophore in the x - y planes will be represented equally. However, in the case of the TM modes there is a small z component of the E field, so the dichroism of the pigments must be taken into account. A conservatively small estimate of the axial dichroism of the pigments based on an analysis of the dichroism of photoreceptor outer segments stimulated from their sides is 3:1.³⁹ With this information and with a measure of the absorbing ability of the photopigment, we calculated the power absorbed by a double cone. As a measure of the absorbing ability of the pigment, we used the specific optical density of the long-wavelength-sensitive cones of the goldfish ($0.0128 \mu\text{m}^{-1}$ O.D. units at its λ_{max} of 625 nm).⁴⁰ With that value for the specific optical density, we approximated the rate at which energy is absorbed along the z axis by presuming that the x dependence of the rate of absorption is carried only by the dependence on x of the field strength [i.e., that the power decays as $\exp(-Dx)$, where D is a constant equal to $\ln(10)$ times the specific optical density of the pigment]. The conductivity of the medium is thus D/η , where η is the characteristic impedance of the volume. In the determination of η , we used an index of refraction of 1.385, the approximate index of the cone outer segment.¹¹ Integrating the conductivity multiplied by the square of the electric field at each point in the volume gives the absorbed power. Division of the absorbed power by the incident power density results in an effective collecting area for the double cone. For TE modes (which are excited by incident waves polarized along the y axis), we obtain

$$a_{m1} = \frac{2d(1 - e^{-Dl})}{\eta P_{\text{inc}}} \int_{-d/2}^{d/2} |E_{x,m}(x)|^2 dx. \quad (10)$$

For TM modes (which are excited by light polarized along the x axis) we obtain

$$a_{m1} = \frac{2d(1 - e^{-Dl})}{\eta P_{\text{inc}}} \int_{-d/2}^{d/2} \left[|E_{x,m}(x)|^2 + \frac{|E_{z,m}(x)|^2}{3} \right] dx, \quad (11)$$

where the division by 3 of the energy in the longitudinal field component represents the effect of the photopigment's dichroism. In Eqs. (10) and (11), P_{inc} is the incident power flux density, l is the length of the outer segment, and d is the thickness of the guide—the distance between which $n \approx 1.33$ —along the x axis. The factor of $2d$ outside the integrands appears as a consequence of the integration from $-d$ to d along the y axis. Initially d was fixed at $7 \mu\text{m}$, but in later analyses we allowed it to vary in order to determine the model's sensitivity to that parameter.

Finally, we defined the local polarization contrast:

$$C_{\text{pol}} = \frac{a_1 - a_{\perp}}{(a_1 + a_{\perp})/2}. \quad (12)$$

Because of the orthogonality of the modes along the z axis, we can define the terms of Eq. (12) simply: $a_1 = \sum_m a_{m1}$ and $a_{\perp} = \sum_m a_{m\perp}$.

The denominator of Eq. (12) is proportional to the average quantal absorption rate of two adjacent orthogonal photoreceptors (see Figs. 2 and 3) under a patch of incident radiation uniformly polarized along the x axis of one of them (and hence along the y axis of the other). The numerator is proportional to the difference between the quantal absorption rates of each of these cells.

3. NUMERICAL RESULTS OF THE GRADED-INDEX MODEL

A. Comparison with the Step-Index Model

The electric fields excited by x and y polarized incident fields have nearly the same magnitude (cf. the values of the a_m 's resulting from the integration of the electric fields in Table 1). However, the magnitudes are different, and this difference is quite possibly large enough to be exploited by a fish's nervous system. Given the parameters $n(x)|_{x=3.5 \mu\text{m}} = 1.33$ and $n_{\text{avg}} = 1.39$, C_{pol} is 1.6% when the incident wavelength is 620 nm (λ_{max} of the pigment is 621 ± 1 nm).⁷

In order to determine what the graded-index profile gains in polarization sensitivity relative to a step-index model, we performed a similar analysis for a guide with a step profile that had the same thickness and average refractive index:

$$\begin{aligned} n &= 1.39 & |x| < 3.5 \mu\text{m}, \\ n &= 1.33 & |x| \geq 3.5 \mu\text{m}. \end{aligned} \quad (13)$$

The procedure for determining C_{pol} was essentially the same. However, in this case there is no ambiguity in the decision regarding whether a mode is guided: the β 's are found from transcendental equations that have a finite number of real values at any given wavelength.⁴¹ Just as in the graded-index-profile model, there are five even-symmetric modes propagating for each x -polarized and y -polarized incident beam with free-space wavelength of 620 nm. The value of C_{pol} obtained from the analysis of the step-profile model at this wavelength is 0.32%; the graded-index model is thus five times as sensitive to polarization as the step-profile model.

B. Wavelength Dependence of Polarization Sensitivity

The differential polarization sensitivity of the green sunfish declines at 690 nm.⁶ We wished to explore the possibility that this might be explained by our model of the double cones' ability to guide light. Figure 6 is a plot of C_{pol} versus the free-space wavelength (λ) of incident radiation for both the graded- and the step-index models. In the graded-index model with the parameters determined above, the power available for phototransduction at relevant wavelengths is always larger when the incident light is polarized along the y axis (C_{pol} is always positive); however, there are discontinuities in $C_{\text{pol}}(\lambda)$ that result from the loss of propagating modes. At discrete wavelengths,

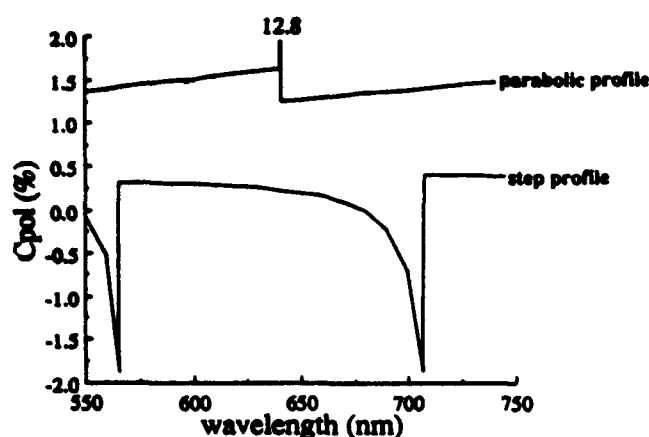


Fig. 6. Polarization contrast as a function of wavelength for one-dimensional parabolic-index and step-index-profile models. C_{pol} is defined by Eq. (11) and is meant to be an indication of the model's preference for one polarization over the other. Positive and negative values indicate a preference for electric fields polarized along the y axis and the x axis, respectively. For the graded-index model, $n_{max} = 1.42$ and $x_0 = 10.0 \mu\text{m}$ in Eq. (3). For the step-index model, n is 1.39 when $|x| < 3.5 \mu\text{m}$ and is 1.33 else. Note that for some wavelengths C_{pol} is negative in the case of the step-index model, whereas this condition never obtains in the graded-index model. In the graded-index model there is a brief interval near 640 nm where y -polarized radiation excites one additional mode compared with x -polarized radiation. At this point C_{pol} leaps to 12.8%; the spike is clipped so that the rest of each function can be shown at a suitable scale.

modes get cut off such that fewer guided modes propagate at longer wavelengths. However, the power available for phototransduction from the TE modes rises more quickly than that for the corresponding TM modes. Just before two corresponding TE and TM modes are cut off, the difference in power that they capture from the two orthogonal incident polarizations becomes substantial. After a given set of modes is cut off, the value of C_{pol} drops, since the remaining set of modes is not so sensitive to polarization. As the wavelength is increased further, C_{pol} increases again until the next-lower set of modes becomes cut off. Another distinctive feature of the plot in Fig. 6 is the spike at the cutoff frequency of one of the TM modes. The spike arises in the graded-index model because each TM mode is cut off at a slightly shorter wavelength than is the corresponding TE mode. Over a short range of wavelengths, the number of propagating TE modes is one greater than the number of propagating TM modes. For this set of parameters the spike is only 0.4 nm wide, however, so we doubt that it could significantly affect the polarization-analyzing capability of the structure given natural excitation, which is typically broadband.⁴³

Contrast the wavelength dependence of the graded-index model with that of the step-index model in the lower part of Fig. 6. The first notable difference is that C_{pol} is significantly smaller for the step-index than for the graded-index model. The second feature of note is that, in the step-index model, C_{pol} reverses sign at some wavelengths. In parts of the spectrum, the energy extracted by the chromophores from light polarized along the x axis is greater than that extracted from light polarized along the y axis. Notice also that there are no spikes in this plot, because in the step-index slab the corresponding TE and TM modes are cut off at the same wavelength.

C. Sensitivity of the Model to Variations in n_{max} and x_0
We calculated the effect of a higher average refractive index by increasing the value of the maximum refractive index [n_{max} in Eq. (2) *et seq.*]. Given that the index of refraction arises principally from proteins and lipids within the cytoplasm, n_{max} is unlikely to be much greater than 1.6.²⁶ However, given those constituents, it may well be higher than our original assumption of 1.42. We therefore repeated the calculations for various values of n_{max} between 1.42 and 1.6 and plotted them in Fig. 7. For these calculations we retained the constraint that $n(x)|_{x=3.5 \mu\text{m}} = 1.33$; so, as n_{max} increased, x_0 decreased (i.e., n fell off with x at a steeper rate). We continued to define the cutoff point in the same fashion (modes were cut off if their effective index was less than 1.33) and considered d in Eqs. (10) and (11) to be $7 \mu\text{m}$. Given these stipulations, as n_{max} increases, the number of modes propagating at each wavelength increases, or at least remains the same. The relative differences between a_{m1} and a_{m2} are larger for each of the corresponding modes, however, so C_{pol} is larger at each wavelength (except at the spikes). As more modes are propagating, there are more modes to get cut off, so $C_{pol}(\lambda)$ has more jumps in it when n_{max} is larger. However, since individual modes do not contribute so much to the total absorbed energy, the relative magnitudes of the jumps are not as large for the larger values of n_{max} .

Because the value of the thickness that we used [d in Eqs. (10) and (11)] was based on an upper limit for the cross section of an inner segment, we wanted to determine how polarization contrast would behave in a smaller structure. Another reason for determining this was that we believed that it might be more appropriate to think of the ellipsoid rather than the entire inner segment as the guiding structure. Since the boundaries of the ellipsoid are contained within the boundaries of the cytoplasmic envelope, the ellipsoid always presents a smaller cross section than does the inner segment in a given section. We explored the effect of a smaller size by fixing n_{max} at 1.42 but choosing a smaller value of x at which to pin the index at 1.33. The narrowest portion of the inner segment is the scleral end, just before the junction with the outer seg-

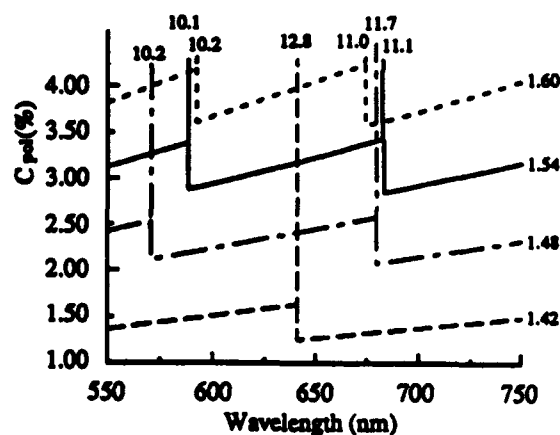


Fig. 7. Polarization contrast as a function of wavelength for different values of maximum index in the parabolic-profile model. In each case, the index profile satisfies Eq. (3) with x_0 set such that $n = 1.33$. The values of n_{max} are depicted at the right of the curves. As in Fig. 6, the number at the top of each spike represents that value to which C_{pol} jumps at that wavelength for the cropped curves.

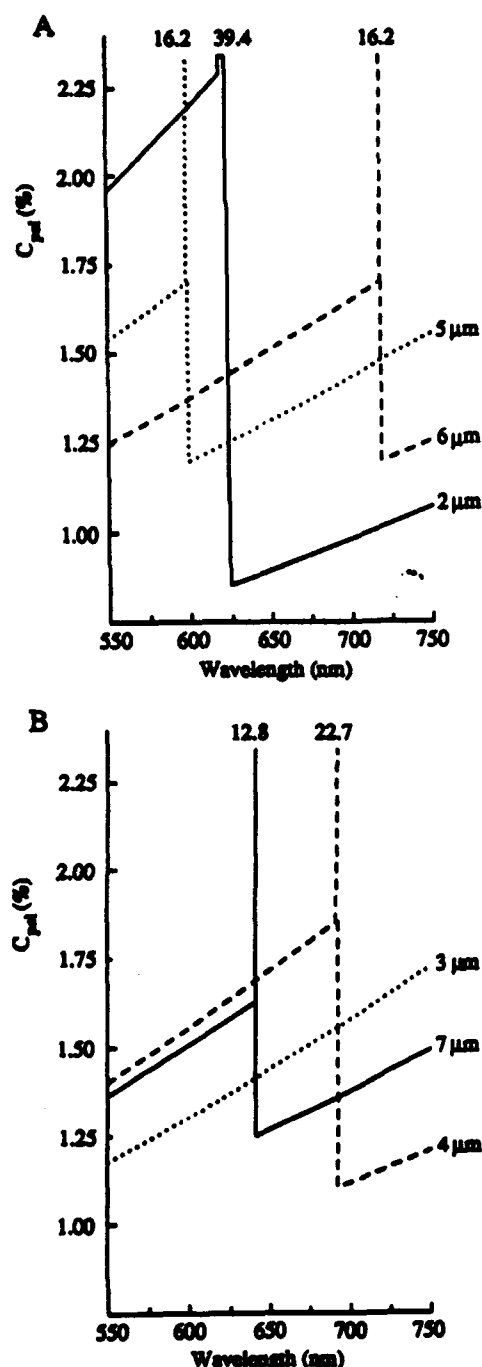


Fig. 8. Polarization contrast as a function of wavelength for different values of thickness in the parabolic-profile model. For ease of viewing, the curves are plotted on two different sets of axes (A and B). For each curve, the index profile satisfies Eq. (3) with $n_{\text{max}} = 1.42$. The values of $|x|$ where $n = 1.33$ are considered the walls of the guide such that the thickness is twice that value. Depicted at the right of each curve is this thickness. As in Figs. 6 and 7, the number at the top of each spike represents the value to which C_{pol} jumps at that wavelength for the cropped curves. For the curve with thickness equal to $2 \mu\text{m}$, the spike is 4 nm wide but is roughly flat, with $C_{\text{pol}} = 39.4\%$. All other spikes are less than 1 nm wide.

ment (see Fig. 1). At this region of the double cone, the ellipsoid may be as small 2 or $3 \mu\text{m}$ wide along the shortest axis. We therefore chose to perform the calculations again for values of d between 2 and $7 \mu\text{m}$. The results of

these calculations are displayed in Fig. 8. As expected, fewer modes propagate as the thickness of the waveguide approaches the size of the wavelength of incident light. When fewer modes are propagating, the loss of a single mode has a much greater effect on C_{pol} ; thus general statements about the usefulness of smaller structures are somewhat more problematic than statements about changes in n_{max} . Decreasing d also makes the spikes tend to become higher and wider. The spike in the case where $d = 2 \mu\text{m}$ jumps to nearly 40% and is 4 nm wide. Since this spike is near the wavelength of maximum absorption for the double-cone pigment, it might have a large effect on the polarization-analyzing ability of the photoreceptor. Therefore in the next paragraph we develop another quantity that incorporates a consideration of the double cones' sensitivity across wavelength.

Broadband polarization contrast. To estimate the effect of broadband polarized light on the relative polarization difference in outputs between orthogonal double cones in the sunfish retina, we define the quantity

$$\bar{C}_{\text{pol}} = \frac{\int_{550}^{750} S(\lambda) a_1(\lambda) d\lambda - \int_{550}^{750} S(\lambda) a_2(\lambda) d\lambda}{\left[\int_{550}^{750} S(\lambda) a_1(\lambda) d\lambda + \int_{550}^{750} S(\lambda) a_2(\lambda) d\lambda \right] / 2}, \quad (14)$$

where λ is the free-space wavelength in nanometers and $S(\lambda)$ is the action spectrum of the double-cone pigment (data collected for Ref. 7, and courtesy of Allen Dearry).⁴³ The P_{inc} used in the determination of the a 's was assumed to be a constant across wavelength. The values of \bar{C}_{pol} thus calculated can be found in Tables 2 and 3.

Table 2. Integration of Differential Polarization Sensitivity: d Fixed at $7 \mu\text{m}$ ^a

n_{max}	\bar{C}_{pol} (%) ^b
1.42	1.460
1.45	1.915
1.48	2.341
1.51	2.737
1.54	3.146
1.57	3.557
1.60	3.966

^aAs in the plots of Fig. 7.

^b \bar{C}_{pol} is defined in Eq. (14). In essence it is a measure of the contrast generated by a pair of orthogonal double cones stimulated by a broadband beam of light, linearly polarized parallel to the long axis of the cross section of one of those cones.

Table 3. Integration of Differential Polarization Sensitivity: n_{max} Fixed at 1.42 ^a

d (μm)	\bar{C}_{pol} (%) ^b
2	2.742
3	1.388
4	1.647
5	1.527
6	1.454
7	1.460

^aAs in the plots of Fig. 8.

^b \bar{C}_{pol} is defined in Eq. (14).

4. DISCUSSION AND CONCLUSIONS

A. Resolution of Three Puzzles

We found that a graded-index model of the sunfish double-cone inner segment predicts the inner segment to guide light in a polarization-dependent manner. We hypothesize that such polarization-dependent guiding, or geometric birefringence, could provide the physical basis for differential polarization sensitivity in many vertebrates. This hypothesis links and could resolve three long-standing puzzles: (1) the puzzle of double cones, (2) the puzzle of double-cone mosaics, and (3) the puzzle of vertebrate polarization sensitivity.

The puzzle of double cones. In discussing double cones, Walls states (p. 58 of Ref. 9) that "the puzzle [that double cones] present is particularly irritating because they are so very widespread among vertebrates," and that "They have unfortunately not greatly interested visual physiologists since the latter have their attention focussed upon the human retina, in which double cones are lacking." In the 50 years intervening since Walls wrote these statements, there has been no hypothesis that attributes to double cones a utility distinct from that of single photoreceptors. The hypothesis that double cones function to take advantage of polarization, a fundamental property of light, is appealing. If this hypothesis is correct, it suggests that many retinas take advantage of a wealth of information contained in the polarization of light constituting a visual scene, information of which we are only beginning to become aware.⁴⁴⁻⁴⁷

The puzzle of double-cone mosaics. The regularity of the double-cone mosaics in many vertebrates is striking (see Refs. 15-18 and also Fig. 3). It has been hypothesized that these mosaics form the basis of a movement-detection system.⁴⁸ However, motion detection by retinas that have no double cones is well established.⁴⁹ More important, given our conclusion that double cones guide light as unitary structures, the double-cone mosaic would be less suitable for motion detection than a similar retinal mosaic with each double cone replaced by two single cones. Motion detection requires the comparison of signals from neighboring receptors. Analysis of Figs. 1 and 2 leads to the conclusion that light impinging upon one of the members of a double-cone pair will be guided into the outer segments of both members, so a comparison of the responses of the members of a double cone would be less informative about motion than comparison of the responses of single cones with the same packing density. On the contrary, the puzzle of the orderly mosaics of double cones may come into sharper focus in light of the hypothesis that double cones are geometric birefringent polarization analyzers. Under this hypothesis the double-cone mosaics could serve as the input for the calculation of a polarization-contrast or -difference image, analogous to a color-contrast image computed by color-opponent cells (see below).

Although the regularity of teleost double-cone mosaics has suggested to others a function in polarization,⁵⁰ the general consequences of this idea seem not to have been pursued. One such consequence is that, in addition to elucidating a role for the square mosaics such as in sunfish, the hypothesis also provides an explanation for the unusual mosaics described by Lyall in the pike⁵¹ and by Walls in the scorpion fish.⁹ In these animals the long axes of

adjacent double cones are offset from each other by 60°. Under the hypothesis that double cones are birefringent polarization analyzers, the mosaic of the pike's retina contains a three-channel polarization-analyzing system analogous to a trichromatic color-vision system (see Ref. 19).

The puzzle of differential polarization sensitivity. Waterman's discovery nearly 35 years ago⁵² and subsequent research demonstrating vertebrate polarization sensitivity¹⁻⁸ have given us the puzzle of a capacity, polarization sensitivity, with no established biophysical mechanism (there is, however, one notable exception in which the mechanism has been established).⁵³ It has been shown through a variety of techniques that the photoreceptors of primates dynamically orient their longitudinal axes toward the exit pupil of the eye.⁵⁴⁻⁵⁶ This orientation serves to maximize the light guided to the outer segments, since off-axis light is ineffectively trapped by photoreceptor inner segments, a phenomenon that explains the Stiles-Crawford effect of the first kind.⁵⁹ However, such orientation of the photoreceptors toward the exit pupil also minimizes the photoreceptors' potential use of the dichroism inherent in the photopigments and outer segment disks for polarization discrimination.⁶⁰ This is so because the E-vector of axially guided light is parallel primarily to the planes of the outer segment disks, in the same planes as the axes of the chromophores. Although it has yet to be established that the longitudinal axes of fish photoreceptors are oriented toward their entrance pupils, it seems likely, on the grounds of optimization of visual sensitivity, that they are. Certainly, the establishment of waveguiding behavior in teleost cones¹³ and the measured directional sensitivity of turtle cones⁶¹ suggest that photoreceptor orientation in these animals will follow a pattern similar to that established in primates.

Nonetheless, some researchers have hypothesized that the dichroism of the photopigments *in situ* could serve for polarization detection by the capture of light that is not propagating radially through photoreceptors. For example, it has been proposed that polarization detection might occur in the embryonic fissure, a prominent structure in many fish.⁶² In this region of the retina, light may strike photoreceptors from the sides, allowing the photoreceptors to make use of the dichroism conferred by the stacking of the disks and the transition moments of the photopigments. However, differential polarization sensitivity was demonstrated in the sunfish when the stimulus was restricted to a region of the retina remote from this fissure.⁶ In the remainder of this discussion we explore ramifications of the hypotheses proposed here, that the inner segments of the photoreceptors in the green sunfish have a graded refractive-index profile and that the three-dimensional shape of this profile gives the photoreceptors sufficient geometric birefringence for that birefringence to serve as a biophysical basis for polarization sensitivity.

B. Graded-Index-Profile Waveguide Model of the Double-Cone Inner Segment

Exclusion of the step-index model. With the size and refractive indices expected for the green sunfish double-cone inner segment, the polarization contrast of the step-index model was approximately 0.3% for wavelengths ranging from 570 to 620 nm. It is possible that an animal could

take advantage of such small differences between the quantal catch rates of its different cone classes: in rhesus macaques the increment threshold for a small monochromatic flash on a 30,000-Td white adapting background is reached when the chromatic contrast between the long- versus middle-wavelength-sensitive cones is 0.28% or 0.5%.⁶³ For humans who are light adapted to a less-intense field, however, the just-detectable chromatic contrast between the long- and middle-wavelength-sensitive cones is approximately 4%.⁶⁴ Thus we doubt that a sunfish could find a maximal cone-contrast difference of 0.3% in its double cones generally useful, given that reflected light from natural targets is unlikely to be perfectly polarized.

An additional argument against the step-index guide can be based on the sign reversals of C_{pol} (see Fig. 6). Such sign reversals would decrease the utility of a double-cone differencing mechanism in real-world conditions, in which radiation tends to be broadband and polarization is a weak function of wavelength. Within a photoreceptor, polarization sensitivity at specific wavelengths will be offset by any opposite-signed polarization sensitivity at other wavelengths.

Basis for geometric birefringence. The evidence for a graded-index profile in sunfish double cones suggested to us that, despite their relatively large size, the double cones might be polarization sensitive as a result of geometric birefringence. When a dielectric waveguide is composed of a nonchiral and isotropic material, its polarization properties depend only on its shape. However, the shape of a waveguide is generally important for polarization-dependent behavior only when the dimensions of the guide are comparable with the wavelength of incident radiation. The narrowest dimensions of the sunfish double-cone cross sections are typically 5–10 times the wavelength of physiologically relevant light. If the index is graded in the manner that we propose, however, then the guided power is concentrated closer to the central axis of the double cone than it would be if the index were homogeneous. Thus a graded-index waveguide is effectively smaller than a step-profile guide with the same outer dimensions and average refractive index, and therefore its polarization contrast is greater.

Absence of extracellular cladding. A striking feature apparent in the electron micrographs of the photoreceptors is that, near the base of the inner segment (the vitreal end), there is an absence of any significant extracellular space. In other words, it appears that the inner segments occupy virtually the entire retinal cross section (see Fig. 1 and Figs. 2b–2e). In most modern analyses of photoreceptors as waveguides, the index profile is assumed to be a step that implicitly requires an extracellular cladding (of thickness comparable with at least the relevant wavelengths, a condition that clearly is not met; see the 620-nm scale bar in Fig. 3a) in order to sustain bound modes easily. In our mathematical analysis of a waveguide model with a graded-index profile, we have also considered the extracellular region as cladding with a refractive index of 1.33. However, as can be seen from Fig. 5, the excited bound modes are not very sensitive to the presence of this extracellular cladding, since they die out rapidly in the region beyond the waveguide's walls. This is due mainly to the fact that in this graded-index-profile model the power of

a mode is concentrated near the guide axis where the index of refraction is the highest. This might suggest a new approach to the modeling of photoreceptor waveguides and has ramifications for the analysis of visual acuity, our next topic.

Possible role in visual acuity. A factor that potentially limits visual acuity in any species is the interphotoreceptor spacing: for maximal acuity, photoreceptors of any fixed size should be tightly packed. Indeed, the spacing between photoreceptors is thought to be the major factor limiting acuity in fish visual systems^{65–68} and perhaps in a variety of other animals, including humans (under some conditions).^{69,70} Tight packing, however, necessarily increases energy coupling between receptors, reducing contrast between adjacent cells and hence reducing visual acuity. Perhaps the greatest advantage of a graded-index profile is the concentration of power near the central guide axis. This power concentration may serve to isolate photoreceptors optically from one another, while permitting maximal packing. A graded refractive-index-profile guide draws light toward its center, reducing coupling and permitting higher acuity for a given receptor size and spacing. This advantage of a graded-index profile does not depend on the noncircular cross sections of the double cones. It would also be conferred on the single cones, which, as seen in Fig. 2, also exhibit a differential electron density across their ellipsoids.

Reduction of backreflections by inner segments. In both single and double cones, the electron density apparently rises and then levels off in the progression from the base of the ellipsoid to the base of the outer segments (see Fig. 1). An advantage conferred by such z -axis gradation is a reduction in the reflection of axially propagating light. Sharp changes in refractive index represent impedance boundaries that produce backreflections. A gradual increase in refractive index reduces these backreflections. Many insect ommatidia are adapted to take advantage of this effect; dimples on the surfaces of their corneas serve as antireflection coatings by reducing the rate at which the refractive index changes as light travels into the animals' eyes.^{71,72} Sunfish photoreceptors appear to take advantage of the same principle in their photoreceptor inner segments.

Combined with the gradation in index along the z axis, the x and y axes' gradation may reduce backscattering of nonparaxial light. Fish have large pupils and nearly spherical lenses. The numerical aperture of the goldfish eye is approximately 0.44,⁶⁶ allowing the photoreceptors to collect light incident up to $\pm 19^\circ$ off of their longitudinal axes.⁷³ For reduction of the reflection at an interface, it is desirable to grade the index slowly in the direction along which light is propagating. Thus the three-dimensional index profile of sunfish cones may minimize the reflection of light over a large entrance aperture while also concentrating the guided light near the center of the guiding structure.

C. Role of the Double-Cone Mosaic: A Basis for Polarization Opponency

Figure 9 diagrams a neural mechanism by which large differential polarization sensitivity can arise from two populations of cells whose sensitivity is a weakly modulated function of polarization. The two sinusoids (dashed

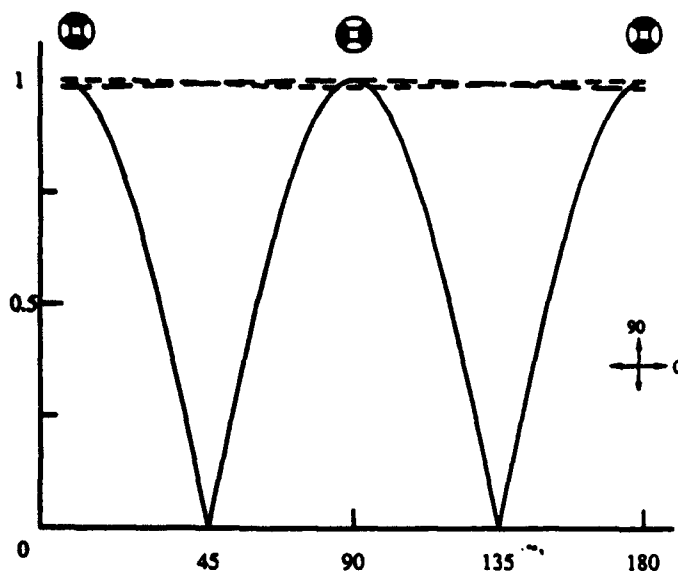


Fig. 2. Opponency between the outputs of two orientation classes of double cone can drastically affect the differential polarization sensitivity of the whole animal. The output of a double cone might be only weakly modulated by polarization, as indicated by the two dashed curves at the top. The shading in the schematic double cones indicates which orientation class should be maximally stimulated at those angles. The large solid curve in the figure represents the unsigned difference between the outputs of the two sets of double cones. Each of the three curves is normalized according to its maximum output.

curves) indicate the response of individual double cones as a function of polarization angle to linearly polarized light of constant intensity, as computed for Table 1. The schematic images of a double-cone tetrad indicate which cells give the largest response at their respective maxima. The solid curve represents the absolute value of the difference between the outputs of the receptors, normalized to the maximum difference. An inner retinal neuron that receives output from the receptors in an opponent fashion would exhibit responses with this magnitude profile, and measurements of an animal's sensitivity could be expected to follow such a pattern. Evidence for polarization opponency in the sunfish retina has been obtained in behavioral experiments.⁶ Furthermore, although pure polarization-opponent cells⁷⁴ have yet to be found in electrophysiological experiments in a vertebrate, they have been predicted to exist in arthropods and have been found in the cricket.⁷⁵ We predict that similarly responsive cells will be found in the retina of a vertebrate.

ACKNOWLEDGMENTS

We thank Jay M. Enoch for helpful comments and suggestions, David A. Cameron for useful comments on earlier versions of the manuscript, Scott Tyo for assistance in the preparation of Fig. 4, and Allen Dearry for the spectral-sensitivity data that we used to generate Tables 2 and 3. This work was supported by National Institutes of Health grant EY00168 to S. S. Easter, Jr., and National Institutes of Health grant EY08260 and U.S. Office of Naval Research grant N00014-89-J-1903 to E. N. Pugh, Jr.

REFERENCES AND NOTES

1. R. B. Forward, Jr., and T. H. Waterman, "Evidence for E-vector and light intensity pattern discrimination by the

- teleost *Dermogenys*," *J. Compar. Physiol.* **87**, 189-202 (1973).
2. H. Kleerekoper, J. H. Matis, A. M. Timms, and P. Genaler, "Locomotor response of the goldfish to polarized light and its E-vector," *J. Compar. Physiol.* **86**, 27-36 (1973).
3. T. H. Waterman, "Polarization sensitivity," in *Comparative Physiology and Evolution of Vision in Invertebrates B: Invertebrate Visual Centers and Behavior I*, H. Autrum, ed., Vol. VII/6B of Handbook of Sensory Physiology (Springer-Verlag, Berlin, 1981).
4. K. P. Able, "Skylight polarization patterns at dusk influence migratory orientation in birds," *Nature (London)* **299**, 550-551 (1982).
5. C. W. Hawryshyn, M. G. Arnold, E. Bowering, and R. L. Cole, "Spatial orientation of rainbow trout to plane-polarized light: the ontogeny of E-vector discrimination and spectral sensitivity characteristics," *J. Compar. Physiol. A* **166**, 565-574 (1990).
6. D. A. Cameron and E. N. Pugh, Jr., "Double cones as a basis for a new type of polarization vision in vertebrates," *Nature (London)* **353**, 161-164 (1991).
7. A. Dearry and R. B. Barlow, "Circadian rhythms in the green sunfish retina," *J. Gen. Physiol.* **89**, 745-770 (1987).
8. Although there has been considerable discussion about the nomenclature of teleost photoreceptors, and many would refer to the structures in question as identical twin cones, we here use double cone as the generic term for any paired cone.
9. G. L. Walls, *The Vertebrate Eye and Its Adaptive Radiation* (Cranbrook, Bloomfield Hills, Mich., 1942).
10. C. R. Braekevelt, "Fine structure of the retinal pigment epithelium and photoreceptor cells of an Australian marsupial *Setonix brachyurus*," *Can. J. Zool.* **51**, 1093-1111 (1972).
11. R. L. Sidman, "The structure and concentration of solids in photoreceptor cells studied by refractometry and interference microscopy," *J. Biophys. Biochem. Cytol.* **3**, 15-33 (1957).
12. J. M. Enoch, "Visualization of waveguide modes in retinal receptors," *Am. J. Ophthalmol.* **51**, 1107-1118 (1961).
13. F. L. Tobey, J. M. Enoch, and J. H. Scandrett, "Experimentally determined optical properties of goldfish cones and rods," *Invest. Ophthalmol.* **14**, 7-23 (1975).
14. Traditionally birefringence refers to the property that the speed of light through a medium or structure is a function of that light's polarization. This is true for our case as well, but in this paper we focus on a consequence of this difference in propagation velocity: the polarization dependence of light's ability to excite the photoreceptor.
15. D. A. Cameron and S. S. Easter, Jr., "The cone photoreceptor mosaic of the green sunfish, *Lepomis cyanellus*," *Vis. Neurosci.* **10**, 375-384 (1993).
16. M. A. Ali and M. A. Anstil, *Retinas of Fishes* (Springer-Verlag, New York, 1976).
17. K. Engström, "Cone types and cone arrangements in teleost retinas," *Acta Zool.* **44**, 179-243 (1963).
18. K. Engström, "On the cone mosaic of the retina of *Parus major*," *Acta Zool.* **39**, 65-69 (1958).
19. G. D. Bernard and R. Wehner, "Functional similarities between polarization vision and color vision," *Vision Res.* **17**, 1019-1028 (1977).
20. We are not proposing that the double cones' sole function is the analysis of optical polarization. Within the retina the signals emerging from the cones may be processed in a variety of ways, and only those that subtract the signals from orthogonal cones will be useful for polarization. Higher-order cells that sum signals from adjacent orthogonal receptors will be polarization blind, but it can be stated with confidence that such cells must exist, to account for the sunfish's sensitivity to light at all angles of linear polarization. If the only information channel from the double cones to the brain of the fish involved the subtraction of the outputs from adjacent orthogonal receptors, there would be two linear polarization angles at which the fish was completely insensitive. It has been observed that this is not the case (see Ref. 6), so, although polarization may be an important stimulus property in the visual world of the sunfish, it is by no means the only property encoded by the double-cone mosaic.
21. The shape is roughly a prolate spheroid near the vitreal end of single cones, in which it was first described. In trans-

- verse sections of double cones, the cytoplasmic envelope and ellipsoid are also roughly elliptical, and it is to these cross sections that we refer when describing the double cones as having elliptical cross sections.
22. T. Ishikawa and E. Yamada, "Atypical mitochondria in the ellipsoid of the photoreceptor cells of vertebrate retinas," *Invest. Ophthalmol.* **8**, 302-316 (1969).
 23. T. R. J. Boesomaier, R. O. L. Wong, and A. W. Snyder, "Stiles-Crawford effect in garter snake," *Vision Res.* **29**, 741-746 (1989).
 24. E. R. Berger, "On the mitochondrial origin of oil drops in the retinal double cone inner segments," *J. Ultrastruct. Res.* **14**, 143-157 (1966).
 25. E. F. MacNichol, Jr., Y. W. Kunz, J. S. Levine, F. I. Hárosi, and B. A. Collins, "Ellipsosomes: organelles containing a cytochrome-like pigment in the retinal cones of certain fishes," *Science* **200**, 540-552 (1978).
 26. R. Barer and S. Joseph, "Refractometry of living cells, part 1. Basic principles," *Q. J. Microsc. Sci.* **95**, 399-423 (1954).
 27. P. M. Tannenbaum, "Spectral shaping and waveguide modes in retinal cones," *Vision Res.* **15**, 591-593 (1975).
 28. I. C. Goyal, A. Kumar, A. Sharma, and A. K. Ghatak, "Stiles-Crawford effect: an inhomogeneous waveguide model for human cone-receptor," *Optik* **49**, 39-49 (1977).
 29. We justify this statement with two related facts. First, $|\partial\epsilon/\partial y|$ is only one half as large as $|\partial\epsilon/\partial x|$ at their largest values within our model cell (i.e., at the points where $x = 0$ and $|y| = 7 \mu\text{m}$, for the maximum in $|\partial\epsilon/\partial y|$, and where $|x| = 3.5 \mu\text{m}$ and $y = 0$ for the maximum in $|\partial\epsilon/\partial x|$); second, the condition that $|\partial\epsilon/\partial x|_{x=c} = 4|\partial\epsilon/\partial y|_{y=c}$ (where $c \leq 3.5 \mu\text{m}$) makes the dielectric wall appear to be closer in the x direction than in the y . We readily admit that this particular approximation will cause the model to overestimate the geometric birefringence of the photoreceptor, but we anticipate that this bias will be canceled out by other parameters (e.g., the neglect in index and size variation along the z axis) that would cause the model to underestimate the birefringence in the living cell.
 30. It is a well-known property of two- and three-dimensional waveguides that solutions of the vector wave equation can be broken down into two types; see, for example J. A. Stratton, *Electromagnetic Theory* (McGraw-Hill, New York, 1941). TE, or transverse electric, refers to a solution that has no longitudinal (z) component of the electric-field vector as the wave travels along the guide, while TM, or transverse magnetic, refers to a solution that has no longitudinal magnetic field. In many cases actual propagating waves can be described only by a hybrid or sum of the two types of mode; but in other cases, such as that analyzed in this paper, the two types of solution represent waves that propagate independently of each other.
 31. M. S. Sodha and A. K. Ghatak, *Inhomogeneous Optical Waveguides* (Plenum, New York, 1977).
 32. The effective index is defined as β_m/k_0 , where β_m is the propagation constant of the m th guided mode.
 33. As discussed later in the text, fish photoreceptors actually receive light from relatively large angles. The transmission coefficient of light traveling from a lower to a higher refractive index depends on both the polarization and the incidence angle of the incident radiation. In the Fresnel coefficient approximation, normal incidence is the only incidence angle at which no polarization-dependent transmission occurs. We performed some preliminary calculations to determine the effect of obliquely incident light on the geometric birefringence of our model. Under such illumination the geometric birefringence decreased, despite the fact that such incidence preferentially stimulates higher-order modes (which are closer to cutoff and hence, as shown in the text, more sensitive to polarization). The decrease in geometric birefringence resulted from the diminution of the transmission coefficient for x -polarized radiation. As we make clear in Section 4, we believe that one of the functions of the graded-index profile (along the z axis as well as along the x and y axes) is to decrease reflection by the photoreceptor inner segment, so that in reality the polarization-analyzing capabilities of the photoreceptors may not be as strongly affected by incidence angle as our model suggests.
 34. For a normally incident plane wave, this coefficient specifies that $E_{\text{trans}}/E_{\text{inc}} = 2n_{\text{inc}}/(n_{\text{inc}} + n_{\text{trans}})$, where the subscripts trans and inc on the electric-field strength and indices refer to the values of those variables in the transmitted and the incident media, respectively. n_{trans} varies as a function of x , and thus, in this approximation, so does the intensity of the transmitted wave.
 35. B. R. Horowitz, "Theoretical considerations of the retinal receptor as a waveguide," in *Vertebrate Photoreceptor Optics* J. M. Enoch and F. L. Tobey, eds. (Springer-Verlag, New York, 1981), pp. 219-300.
 36. J. Heller and J. Horwitz, "Photoselection and linear dichroism of retinal isomers and visual pigments," in *Biochemistry and Physiology of Visual Pigments*, H. Langer, ed. (Springer-Verlag, New York, 1973).
 37. R. A. Cone, "Rotational diffusion of rhodopsin in the visual receptor membrane," *Nature (London)* **236**, 39-43 (1972).
 38. B. D. Gupta and T. P. Williams, "Lateral diffusion of visual pigments in toad (*Bufo marinus*), and catfish (*Ictalurus punctatus*) cones," *J. Physiol.* **430**, 483-496 (1990).
 39. Given the numbers found in A. W. Snyder and S. B. Laughlin, "Dichroism and absorption in photoreceptors," *J. Compar. Physiol.* **100**, 101-116 (1976), we believed that 3:1 was a reasonable value; however, other evidence suggests that it could be higher: e.g., F. I. Hárosi and E. F. MacNichol, Jr., in "Dichroic microspectrophotometer: a computer assisted rapid wavelength-scanning photometer for measuring the linear dichroism of single cells," *J. Opt. Soc. Am.* **64**, 903-918 (1974), suggest that a more reasonable estimate (at least in frog rods) might be 5:1. It is difficult to apply these numbers directly to our model, because the measurements come from intact photoreceptors, and what our model needs to take into account is the dichroism of the individual pigments. In an attempt to bias the model away from our preferred conclusion, we have chosen what we believe to be a small value for this dichroism.
 40. F. I. Hárosi and E. F. MacNichol, Jr., "Visual pigments of goldfish cones, spectral properties and dichroism," *J. Gen. Physiol.* **63**, 279-304 (1974).
 41. D. L. Lee, *Electromagnetic Principles of Integrated Optics* (Wiley, New York, 1986).
 42. P. Lennie and M. D'Zmura, "Mechanisms of color vision," *CRC Crit. Rev. Neurobiol.* **3**, 333-400 (1988).
 43. Deary and Barlow did not attempt to measure the specific optical density; they did not adjust their data according to the size of the cells from which they obtained their measurements. It thus was not possible to use these data directly in the generation of the data presented in Table 1.
 44. J. N. Lythgoe and C. C. Hemmings, "Polarized light and underwater vision," *Nature (London)* **213**, 893-894 (1967).
 45. L. B. Wolff, "Polarization-based material classification from specular reflection," *IEEE Trans. Patt. Anal. Mach. Intell.* **13**, 1059-1071 (1990).
 46. L. B. Wolff and T. E. Boulton, "Constraining object features using a polarization reflectance model," *IEEE Trans. Patt. Anal. Mach. Intell.* **13**, 635-657 (1992).
 47. B. F. Jones and P. T. Fairney, "Recognition of shiny dielectric objects by analysing the polarization of reflected light," *Image Vis. Comput.* **7**, 253-258 (1989).
 48. H. J. Wagner, "Vergleichende Untersuchung über das Muster der Sehzellen und Horizontalen in der Teleostier-Retina (Pisces)," *Z. Morphol. Tiere* **72**, 77-130 (1972).
 49. A. Borst and M. Egelhaaf, "Principles of visual motion detection," *Trends Neurosci.* **12**, 297-306 (1989).
 50. T. H. Waterman and R. B. Forward, Jr., "Field evidence for polarized light sensitivity in the fish *Zenarchopterus*," *Nature (London)* **228**, 85-87 (1970).
 51. A. H. Lyall, "Cone arrangements in teleost retinas," *Q. J. Microsc. Sci.* **98**, 189-201 (1957).
 52. T. H. Waterman, "The problem of polarized light sensitivity," *Proc. Intl. Congr. Zool.* **15**, 537-539 (1959).
 53. In one special case in which vertebrate polarization sensitivity is known, the mechanism is clear. In the anchovy [see B. A. Fineran and J. A. C. Nicol, "Studies on the photoreceptors of *Anchoa mitchilli* and *A. hepsetus* (Engraulidae) with particular reference to the cones," *Philos. Trans. R. Soc. London Ser. B* **283**, 25-60 (1978)], the outer segments of

- the cones have a unique shape that allows them to capture light as it propagates parallel to the disks rather than perpendicular to them as it does in all other vertebrates thus far examined.
54. A. M. Laties, "Histological techniques for the study of photoreceptor orientation," *Tissue Cell* 1, 63-81 (1969).
 55. A. M. Laties, P. A. Liebman, and C. E. M. Campbell, "Photoreceptor orientation in the primate eye," *Nature (London)* 218, 172-173 (1968).
 56. A. M. Laties and J. M. Enoch, "An analysis of retinal receptor orientation. I. Angular relationship of neighboring photoreceptors," *Invest. Ophthalmol.* 10, 69-77 (1971).
 57. J. M. Enoch and A. M. Laties, "An analysis of retinal receptor orientation. III. Results of initial psychophysical tests," *Invest. Ophthalmol.* 11, 765-782 (1972).
 58. J. M. Enoch and D. G. Birch, "Inferred positive phototropic activity in human photoreceptors," *Philos. Trans. R. Soc. London Ser. B* 291, 323-351 (1981); but see also J. M. Enoch and D. B. Birch, "Comment on inferred positive phototropic activity in human photoreceptors," *Philos. Trans. R. Soc. London Ser. B* 309, 611-613 (1985).
 59. A. W. Snyder and C. Pask, "The Stiles-Crawford effect—explanation and consequences," *Vision Res.* 13, 1115-1137 (1973).
 60. The possibility that preretinal mechanisms might account for polarization sensitivity can be discounted on the basis of Ref. 6. In that paper it was established that the polarization sensitivity manifested by the animals under photopic conditions was not apparent under scotopic conditions. This fact, in conjunction with the fact that the polarization-sensitivity profile matched the spectral sensitivity of the pigment in the double cones, makes it seem most unlikely that the sensitivity arises from any structures proximal in the light path to the photoreceptors.
 61. D. A. Baylor and R. Fettiplace, "Light path and photon capture in turtle photoreceptors," *J. Physiol.* 248, 433-464 (1975).
 62. Y. Kunz and E. Callaghan, "Embryonic fissures in teleost eyes and their possible role in detection of polarized light," *Trans. Am. Fish. Soc.* 118, 195-202 (1989).
 63. M. Kalloniatis and R. S. Harwerth, "Spectral sensitivity and adaptation characteristics of cone mechanisms under white-light adaptation," *J. Opt. Soc. Am. A* 7, 1912-1928 (1990). In this reference, threshold data are plotted as $\delta L/L$ versus $\delta M/M$, where δL is the quantal catch of the long-wavelength-sensitive cones from the test flash and L is the quantal catch of the long-wavelength-sensitive cones from the adapting background, and similarly for the middle-wavelength-sensitive cones. The contour representing $\delta L/L - \delta M/M = k$ intercepts the $\delta L/L$ axis at $\delta L/L = 0.14\%$, indicating that the constant $k = 0.14\%$ when the adapting light has an intensity of 30,000 Td. Assuming that $M = L$, leads to $(\delta L - \delta M)/(L + M)/2 = 0.28\%$. Similarly, the 0.5% arises from the $\delta M/M - \delta L/L = k$ contour.
 64. We used values from D. J. Calkins, J. E. Thornton, and E. N. Pugh, Jr., "Monochromatism determined at a long-wavelength/middle-wavelength cone-antagonistic locus," *Vis. Res.* 32, 2349-2367 (1992), to calculate $2(k_1\delta M - k_2\delta L)/(L + M)$, where L and M are the responses of the long- and middle-wavelength-sensitive cones, respectively, to the steady background, δM and δL are the cones' responses to the stimulus field, and k_1 and k_2 are constants.
 65. W. N. Charman and J. Tucker, "The optical system of the goldfish eye," *Vision Res.* 13, 1-8 (1973).
 66. R. J. Pumphrey, "Concerning vision," in *The Cell and the Organism*, J. A. Ramsay and V. B. Wigglesworth, eds. (Cambridge U. Press, Cambridge, 1961).
 67. J. D. Sadler, "The focal length of the fish eye lens and visual acuity," *Vision Res.* 13, 417-423 (1973).
 68. N. G. Hairston, Jr., K. T. Li, and S. S. Easter, Jr., "Fish vision and the detection of planktonic prey," *Science* 218, 1240-1242 (1982).
 69. J. Hirach and W. H. Miller, "Does cone positional disorder limit resolution?" *J. Opt. Soc. Am. A* 4, 1481-1492 (1987).
 70. D. R. Williams and N. J. Coletta, "Cone spacing and the visual resolution limit," *J. Opt. Soc. Am. A* 4, 1514-1523 (1987).
 71. W. H. Miller, "Ocular optical filtering," in *Comparative Physiology and Evolution of Vision in Invertebrates A: Invertebrate Photoreceptors*, H. Autrum, ed., Vol. VII/8A of *Handbook of Sensory Physiology* (Springer-Verlag, New York, 1979), pp. 69-143.
 72. S. Dey, "Scanning electron microscopic detection of corneal anti-reflection coating in the grasshopper, *Epacromia dorsalis*, and its physiological significance," *Vision Res.* 28, 975-977 (1988).
 73. The numerical aperture of the goldfish eye is given as 0.44 in Ref. 65. The $\pm 19^\circ$ assumes a refractive index of 1.337 in the vitreous.
 74. By pure polarization opponent we mean a cell that receives opposite-signed inputs from two photoreceptors with the same spectral response properties but different polarization response properties.
 75. T. Labhart, "Polarization-opponent interneurons in the insect visual system," *Nature (London)* 331, 435-437 (1988).